



Significant role of physical transport in the marine carbon monoxide (CO) cycle: observations in the East Sea (Sea of Japan), the western North Pacific, and the Bering Sea in summer

Young Shin Kwon^{1,2}, Tae Siek Rhee², Hyun-Cheol Kim³, and Hyoun-Woo Kang⁴

¹Ocean Climate Response & Ecosystem Research Department, Korea Institute of Ocean Sciences and Technology, Busan, 49111, Korea

²Division of Ocean and Atmospheric Sciences, Korea Polar Research Institute, Incheon, 21990, Korea

³Center of Remote Sensing & GIS, Korea Polar Research Institute, Incheon, 21990, Korea

⁴Ocean Climate Solutions Research Division, Korea Institute of Ocean Sciences and Technology, Busan, 49111, Korea

Correspondence: Tae Siek Rhee (rhee@kopri.re.kr)

Received: 8 October 2023 – Discussion started: 11 October 2023

Revised: 23 February 2024 – Accepted: 23 February 2024 – Published: 15 April 2024

Abstract. The carbon monoxide (CO) in the marine boundary layer and in the surface waters and water column were measured along the western limb of the North Pacific from the Korean Peninsula to Alaska, USA, in summer 2012. The observation allows us to estimate the CO budgets in the surface mixed layer of the three distinct regimes: the East Sea (Sea of Japan) (ES), the Northwest Pacific (NP), and the Bering Sea (BS). CO photochemical production rates were $56(\pm 15)\mu\text{mol m}^{-2}\text{d}^{-1}$, $27(\pm 3)\mu\text{mol m}^{-2}\text{d}^{-1}$, and $26(\pm 2)\mu\text{mol m}^{-2}\text{d}^{-1}$, while microbial consumption rates were $30(\pm 8)\mu\text{mol m}^{-2}\text{d}^{-1}$, $24(\pm 5)\mu\text{mol m}^{-2}\text{d}^{-1}$, and $63(\pm 19)\mu\text{mol m}^{-2}\text{d}^{-1}$ in the ES, NP, and BS, respectively, both of which are the dominant components of the CO budget in the ocean. The other two known components, air–sea gas exchange and downward mixing, remained negligible (less than $3\mu\text{mol m}^{-2}\text{d}^{-1}$) in all regimes. While the CO budget in the surface mixed layer of the NP was in balance, the CO production surpassed the consumption in the ES, and vice versa in the BS. The significant imbalances in the CO budget in the ES ($25 \pm 17\mu\text{mol m}^{-2}\text{d}^{-1}$) and the BS ($40 \pm 19\mu\text{mol m}^{-2}\text{d}^{-1}$) are suggested to be compensated by external physical transport such as lateral advection, subduction, or ventilation. Notably, the increase in the CO column burden correlated with the imbalance in the CO budget, highlighting the significant role of the physical transport in the marine CO cycles. Our observation, for the first time, un-

derscores the potential importance of physical transport in driving CO dynamics in the marine environment.

1 Introduction

Carbon monoxide (CO) plays a key role in the budget for the hydroxyl (OH) radical in the atmosphere (Weinstock and Niki, 1972; Levy, 1971), which indirectly contributes to global climate change as a considerable range of greenhouse gases, including methane (CH_4), are oxidized by the OH radical in the atmosphere (Daniel and Solomon, 1998). The ocean has long been recognized as a source of atmospheric CO, albeit with large uncertainties in its source strength ($1\text{--}190\text{ Tg CO yr}^{-1}$) (Conte et al., 2019; Erickson, 1989; Bates et al., 1995; Conrad et al., 1982; Stubbins et al., 2006a; Zafiriou et al., 2003; Park and Rhee, 2016), which requires further investigation and understanding of the CO cycle in the ocean.

In the ocean's euphotic zone, CO undergoes production through abiotic photochemical reaction of chromophoric dissolved organic matter (CDOM) and particulate organic matter (Xie and Zafiriou, 2009). The annual global CO photoproduction in the ocean spans an estimated range of $10\text{--}400\text{ Tg CO}$ (Mopper and Kieber, 2000; Zafiriou et al., 2003; Erickson, 1989; Conrad et al., 1982; Fichot and Miller, 2010; Stubbins et al., 2006b). This wide range of estimations is largely attributed to the uneven distribution of CDOM

throughout the world's oceans. CO, as the second most substantial inorganic carbon product after CO₂ in photochemical conversion of dissolved organic carbon, garners significant attention. It serves as a pivotal proxy for assessing the photoproduction of CO₂ and bio-labile organic carbon (Mopper and Kieber, 2000; Miller et al., 2002). Thus, CO holds a prominent position within the context of both the oceanic carbon cycle and the broader realm of global climate change.

In contrast, CO within the ocean's water column experiences removal mechanisms that include microbial consumption, air–sea gas exchange, and vertical dilution. Under normal turbulent conditions at the ocean's surface, microbial consumption emerges as the dominant sink for CO. The rate constants governing microbial consumption of CO exhibit considerable variability, ranging from 0.003 to 1.11 h⁻¹ depending on factors such as location and season (Conrad and Seiler, 1980; Conrad et al., 1982; Johnson and Bates, 1996; Jones, 1991; Ohta, 1997; Xie et al., 2005; Zafiriou et al., 2003; Jones and Amador, 1993). Notably, dissolved CO in the surface ocean tends to be supersaturated with respect to the atmospheric CO concentrations (Seiler and Junge, 1970) resulting in emission from the sea to the air (Conrad and Seiler, 1980). However, the influence of physical mixing within the surface mixed layer becomes apparent when the mixed layer depth exceeds the depth of light penetration depth, rendering photoproduction no longer the dominant driver (Gnanadesikan, 1996; Kettle, 1994).

Efforts to estimate the oceanic source strength of CO encounter significant challenges due to the substantial uncertainties inherent in the marine CO budget. Recent modeling endeavors have aimed at estimating the global-scale CO flux from the ocean surface (Conte et al., 2019). However, these estimations grapple with formidable uncertainties, especially in regions characterized by shallow continental shelves. Additionally, attempts have been made to address these challenges by introducing a new production pathway known as dark production (Xie et al., 2005; Kettle, 2005b; Zhang et al., 2008), which seeks to reconcile the discrepancies between modeled and observed oceanic CO source strength. Nevertheless, the widespread occurrence of dark production at a global scale remains a subject of ongoing debate (Zafiriou et al., 2008). The identification of missing components within the CO budget holds paramount importance, as it can significantly enhance our predictive capabilities, allowing for a better understanding of the dynamic interplay between oceanic CO levels and the broader context of global climate change.

To better understand the CO dynamics in distinct marine environments, we conducted a comprehensive study on the distribution of CO in the water column and the overlying air, the microbial consumption rate, and the CDOM absorbance. In this study, we report a CO budget estimated from these observations and onboard experiments, and compare it with the column burden of CO to examine the controlling factors affecting CO distribution in the water column. While there have been limited observations of dissolved CO in this study

region (Lamontagne, 1979; Nakagawa et al., 2004), our research represents the first comprehensive observational study of CO distribution and the associated source and sink processes within the extensive region encompassing the western limb of the North Pacific.

2 Materials and methods

2.1 Expedition

The SHIPborne Pole-to-Pole Observations (SHIPPO) expedition was carried out on board R/V *Araon* from Incheon, Korea, to Nome, Alaska, USA, over 2 weeks in 2012 (Fig. 1). The cruise track covered the coast surrounding the Korean Peninsula and three ocean provinces: the East Sea (Sea of Japan) (ES), the western limb of the North Pacific (NP), and the Bering Sea (BS). For this study, we focused on the oceanic properties relevant to the marine CO cycle in the ES, NP, and BS, and thus excluded the coastal regions around the Korean Peninsula and near Nome, Alaska, in defining the ocean province (see Fig. 2). Along the cruise track, we occupied two hydrographic stations in the ES – one on the northern fringe of the Ulleung Basin between the islands of Ulleung-do and Dokdo Islands, and the other on Yamato Rise – six stations in the NP spreading from the east of the Tsugaru Strait to the western Aleutian Islands, and three stations in the BS – one at the Bering Slope, another in the inner shelf, and the other near the port in Nome. We excluded station 12 from the BS province, as it is too close to the coast to represent the oceanographic properties of the Bering Sea. The expedition covers characteristic marginal seas, i.e., the ES and BS, and the open ocean of the NP.

2.2 Underway CO measurements

A commercially available instrument, RGA-3 (Reduced Gas Analyzer-3; Trace Analytical Inc.), was used to analyze CO with an automated analytical system (Rhee, 2000). The analytical system was calibrated with commercially available calibration gases (49.09 ± 1.16 , 102.0 ± 0.7 , and 912.8 ± 4.7 ppb) during the SHIPPO campaign. The dry mole fractions assigned to these calibration gases were adjusted based on traceable standard gases from NOAA/ES-RL/GMD (NOAA-GMD/WMO 2004 scale). For measuring high CO concentrations (> 1 ppm), the highest concentration of calibration gas was adjusted using Swiss Empa standard gases (Vollmer et al., 2012). To cover a wide range of CO concentrations between the air and surface seawater, two different sizes of sample loops (0.5 and 2 mL) were installed on the 10-port VICI valve. This setup allows us to confidently measure CO concentrations of up to ~ 2 ppm in unknown samples since the concentrations of the standard gases range from ~ 20 to ~ 1800 ppb. Beyond this range of unknown samples, we anticipate an increase in analytical uncertainty. The uncertainties (1σ) associated with the standard

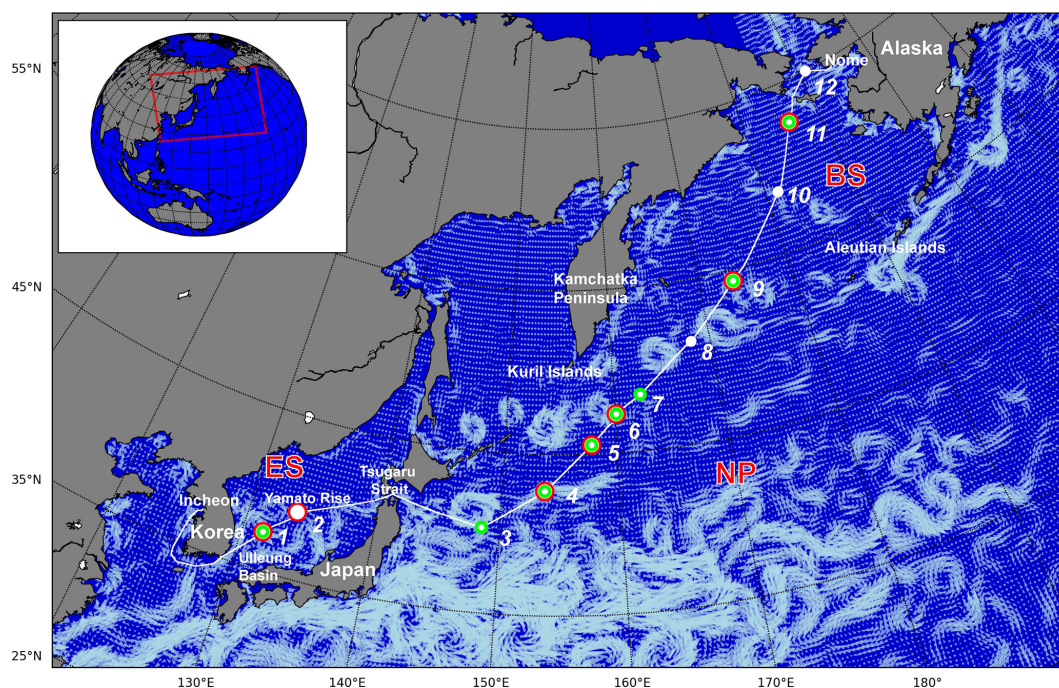


Figure 1. Cruise track (white line) and hydrographic stations (white dots) occupied during the SHIPPO expedition. Dark incubation experiments were conducted at the locations marked by red circles and CDOM absorbance was measured at the locations marked by green circles. The white-blue vectors on the map designate surface mean currents in July 2012 as taken from the OSCAR (Ocean Surface Current Analysis Real-time) database. The red square in the inset indicates the study area.

gases are estimated to be between 0.5 and 1.1 ppb, following the NOAA-GMD/WMO 2004 scale (see Fig. S1 in the Supplement). The detection limit of the system was determined to be 6 ppb ($= 3\sigma$ of blank signals) based on the blank runs applied during discrete sample analysis. To correct for detector signal drift, calibration runs were performed every 40 min during sample analyses.

The ambient air at 29 m above sea level was withdrawn through ~ 100 m-long polyethylene inner-coated aluminum tubing (DEKABON) by a pump (KNF, N026ATE) for atmospheric CO analysis. No contamination from the media was detected (Park and Rhee, 2015). To ensure the reliability of the atmospheric measurements and minimize the potential influence of ship exhaust, we relied on the data reduction previously conducted by Park and Rhee (2015). We selected a specific time window for data quality control based on the criteria they established (refer to Fig. S2 in Park and Rhee, 2015). In brief, the atmospheric CO data were excluded if the relative wind speed (in relation to the ship's speed) was less than 2 kn to prevent potential contamination from stack emissions resulting from local turbulence. Data with a standard deviation exceeding 1 ppb for 1 min were also excluded. Furthermore, data collected with a relative wind direction between 180 and 270°, corresponding to the ship's stack location relative to the air inlet, underwent rigorous screening.

Seawater inlet was mounted on the sea chest located ~ 7 m below the sea surface. Seawater was pumped into a typi-

cal shower-type Weiss equilibrator in which dissolved CO in the seawater was dynamically equilibrated with the CO in the headspace, which was then delivered to the analyzer. The equilibrator was made of opaque polytetrafluoroethylene (Teflon™) and seated in the laboratory. Seawater was continually showered through the headspace at ~ 30 L min $^{-1}$, resulting in the equilibration time of 40 min for CO. The ambient air and the headspace air in the equilibrator were sampled every 45 min. To keep the analyzing system from being wet, a water trap (Sicapent™) was mounted in front of the automated CO analyzing system. No alteration of CO concentration due to mounting the water trap was detected.

2.3 Dissolved CO concentrations in discrete samples

Dissolved CO concentrations in the discrete samples of each hydrographic station were determined by the static equilibrium technique. Seawaters were subsampled in glass jars from the Niskin samplers fired at given depth. A known amount (50 mL) of ultra-pure N₂ gas (99.9999%) was collected using a gas-tight syringe after passing through a Schuetze reagent which oxidizes CO to CO₂ effectively (Brenninkmeijer, 1993; Pathirana et al., 2015). This CO-free N₂ was injected into the glass jars to make headspace. After being shaken vigorously, the glass jars were placed in a thermostat at 20 °C for about 1 h to reach equilibrium between the headspace and the seawater of dissolved CO. Then,

the air in the headspace was analyzed using the same analytical system that was used for underway measurements with manual injection. Dissolved CO concentration, C_w (in nmol kg^{-1}), was determined by applying the following equation based on the conservation of the dissolved CO concentration in the seawater sample collected in the jar (Rhee et al., 2009):

$$C_w = \frac{x_{\text{CO}} \times (P - P_w)}{\rho_w R T} \times \left(\beta \times \frac{T}{273.15} + \frac{V_h}{V_w} \right), \quad (1)$$

where x_{CO} represents the dry mole fraction of dissolved CO (in nmol mol^{-1}), P ambient pressure (in atm), P_w saturated water vapor pressure (in atm), ρ_w density of seawater at a given temperature (in kg L^{-1}), R gas constant ($0.08205601 \text{ L atm mol}^{-1} \text{ K}^{-1}$), T absolute temperature at the sampling time of dissolved gas (in degrees K), V_h volume of the headspace (in mL), and V_w volume of the seawater (in mL). β denotes the Bunsen coefficient of CO solubility which is defined as the volume of CO gas, reduced to STP (0°C 1 atm) contained in a unit volume of water at the temperature of the measurement when the partial pressure of the CO is 1 atm (Wiesenburg and Guinasso, 1979). We calculate β using Eq. (1) in Wiesenburg and Guinasso (1979). The conversion of β to the temperature at which dissolved CO is measured is referred to as the Ostwald coefficient solubility, denoted as L ($= \beta \times T/273.15$), as indicated within the parentheses in Eq. (1).

2.4 Determination of microbial oxidation rate constant

Dark incubation experiments were conducted on board at selected stations to determine the microbial oxidation rate constant of CO (k_{CO}) in unfiltered seawater samples collected in the surface mixed layer. At the selected stations (marked with red circles in Fig. 1), four aliquots of seawater were subsampled into glass jars from a Niskin bottle. To prevent light exposure during sampling, the glass jars were covered with colored cellulose film. These jars were then placed in an aquarium where surface seawater was continuously supplied to maintain a temperature identical to that in the surface mixed layer. Upon collection, one of these sample bottles underwent immediate analysis to measure dissolved CO concentration. Subsequently, the remaining three samples were analyzed at distinct time intervals following the initial sampling. Before analysis, we introduced ultra-pure N_2 gas into each sample bottle to create a headspace following the same procedure outlined in Sect. 2.3. After allowing the samples to equilibrate, we extracted the headspace sample for analysis.

As CO depletion follows quasi-first-order reaction kinetics at ambient CO concentrations (Johnson and Bates, 1996; Jones and Amador, 1993), we fitted the data with the best-fit lines using the following equation:

$$\ln \left(\frac{[\text{CO}]_t}{[\text{CO}]_0} \right) = -k_{\text{CO}} \times t, \quad (2)$$

where t represents time (in h) and k_{CO} is the microbial oxidation rate constant for the reaction (h^{-1}), and $[\text{CO}]_t$ and $[\text{CO}]_0$ denote the CO concentrations at time t and the beginning of the incubation experiment, respectively.

2.5 CDOM analysis

Approximately 200 mL of seawater was subsampled in an amber glass container from a Niskin bottle at selected stations (green circles in Fig. 1). The seawater sample was filtered through $0.45 \mu\text{m}$ filter paper (Advantec). Absorption spectra of the filtrate were obtained using a spectrophotometer (Agilent Cary-100) by scanning the wavelength from 350 to 800 nm. Milli-Q water was used as a reference blank. Baseline offset was corrected by subtracting the average apparent absorbance from 600 to 700 nm from each spectrum.

CDOM absorbance obtained from the instruments on board was converted to the absorption coefficient (a_c ; m^{-1}) by the Beer–Lambert law. Previous studies demonstrated the exponential decay of a_c with an increase in wavelength in the region of ultraviolet and visible light, which can be represented by a_c at a reference wavelength, λ_0 , and spectral slope, S (nm^{-1}) (Bricaud et al., 1981). These two characteristic parameters can be determined by fitting to the following exponential form:

$$a_c(\lambda) = a_c(\lambda_0) \times e^{-S(\lambda-\lambda_0)}. \quad (3)$$

We chose the reference wavelength of 412 nm which is often used in the remote sensing community as a representative of CDOM absorption in the ocean. $a_c(412)$ by CDOM was proven to be a typical linear relation with the CDOM absorption at other wavelengths (Mannino et al., 2014). In addition, this wavelength is often chosen to correct the absorption by CDOM to derive Chl-*a* in remote sensing (e.g., Carder et al., 1999) or to compare the spectral slopes in the CDOM absorption obtained in various regions (e.g., Twardowski et al., 2004).

2.6 Ancillary measurements

Wind speed was measured by an anemometer (model 05106-8M; R.M. Young Co.) installed on the foremast at 29 m above sea level. It was corrected for ship speed and direction to obtain true wind speed (Smith et al., 1999) and then converted to the neutral wind speed at 10 m above sea level of standard height using the bulk air–sea flux algorithm COARE 3.6 (Edson et al., 2013; Fairall et al., 2003). Solar irradiation was measured with an Eppley precision spectral pyranometer (model PSP) integrating radiation over 285–2800 nm. The surface Chl-*a* concentration was measured by a fluorometer (Turner Designs 10-AU) supplying the surface seawater continuously. The values were adjusted to the Chl-*a* concentration determined by a Trilogy laboratory fluorometer (Turner Designs) according to the standard procedure described by Parsons et al. (1984). Sea surface temperature (SST) and sea

surface salinity (SSS) were logged using both a thermosalinograph (SBE-45; Seabird) mounted in the laboratory and a pair of thermometers (SBE-38) mounted on the seawater inlet of the sea chest.

2.7 Calculation of the CO budget terms

Assuming that lateral advection of CO is negligible, dissolved CO concentration ($[CO]$; in nM) in the mixed layer, h (in m), was determined by the sum of the rates of photochemical production (J), air–sea gas exchange (F), vertical diffusion (V) across the bottom of the mixed layer, and microbial oxidation (M):

$$h \frac{d[CO]}{dt} = J + M + F + V. \quad (4)$$

Hence, the unit for J , M , F , and V is $\mu\text{mol m}^{-2} \text{d}^{-1}$. We assume dark production (Zhang et al., 2008) or other unknown processes, including production from particulate carbon and emission by phytoplankton (Xie and Zafiriou, 2009; Gros et al., 2009), to be negligible in the CO budget. We calculated daily budget terms of CO in the surface mixed layer at the stations based on our observed data. Here we defined 1 d as the sum of half a day before and after the time of CTD (conductivity–temperature–depth array of sensors) cast (gray strip in Fig. 2). The CO budget terms were integrated over the mixed layer at the given station (see Fig. S3c and d as an example). Mixed layer depth (MLD) was determined at the shallowest depth below reference depth of 10 m at which the density difference exceeds the density at the reference depth due to a temperature difference of 0.2 °C (de Boyer Montégut, 2004).

2.7.1 Photochemical production

The photochemical production rate (J) was determined by the product of irradiance (I_0), the amount of CDOM (a_c), and the apparent quantum yield (Φ_{CO}) of CDOM, an indicator of the CO production efficiency. Since CDOM is not a chemical compound but rather a moiety of material defined by mechanical criterion, Φ_{CO} varies depending on a variety of environmental conditions. J can be mathematically described as follows:

$$J = \int_{z=0}^{z=\infty} \int_{\lambda_{\min}}^{\lambda_{\max}} I_0(\lambda, 0^-) e^{-k_d(\lambda)z} \times a_c(\lambda, z) \times \Phi_{CO}(\lambda) d\lambda dz, \quad (5)$$

where $I_0(\lambda, 0^-)$ indicates the monochromatic solar irradiance just beneath the air–sea interface, $k_d(\lambda, z)$ the diffuse attenuation coefficient, and $\Phi_{CO}(\lambda, z)$ the apparent quantum yield of CO. The parentheses in Eq. (5) indicate the function of variables, i.e., λ wavelength and z water depth.

We measured irradiance in the short-wavelength range on board, but not individual monochromatic wavelengths. Thus, a model calculation by the tropospheric ultraviolet and visible radiation (TUV) model (<https://www2.acom.>

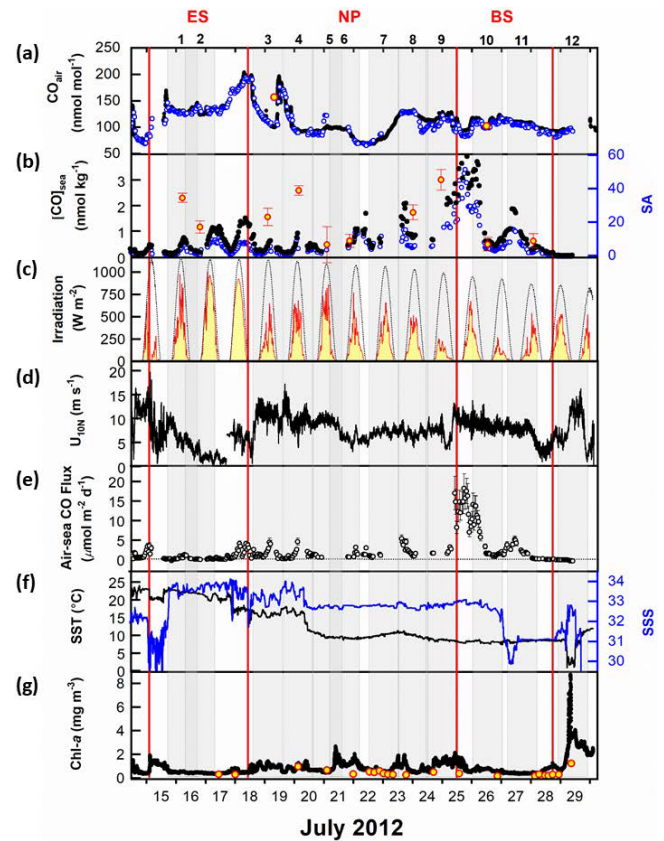


Figure 2. Surface properties observed along the cruise track: (a) mole fractions of CO in the air, (b) dissolved CO concentrations and saturation anomaly in the sea surface mixed layer, (c) observed surface irradiance (solid red line) and modeled clear-sky irradiance (thin dotted line), (d) neutral wind speed at 10 m high, (e) daily sea-to-air CO flux, (f) sea surface temperature (SST) and sea surface salinity (SSS), and (g) chlorophyll-*a* (Chl-*a*) concentrations in the surface waters. Time is given in UTC. In (a), the black circles represent analyses by LGR systems, the blue circles represent RGA-3 analyses, and the two red circles filled with yellow represent the observations at the NOAA/ESRL global network stations, SHM (Shemya Island, Alaska) and CBA (Cold Bay, Alaska). In (b), the red circles filled with yellow represent discrete measurements interpolated at a depth of 7 m at each hydrographic station. In (g), the black dots represent the continuous measurement by the Turner 10-AU fluorometer and the red circles filled with yellow indicate the discrete measurements of Chl-*a*. Individual gray-shaded areas represent 1 d at the given station. The geographical provinces of the ES, NP, and BS are separated by vertical red lines.

ucar.edu/, last access: 1 December 2015) was employed to resolve the irradiance of the monochromatic wavelength between 290 and 800 nm. The total irradiance from TUV was normalized to the observed irradiance to estimate the irradiance on the sea surface. To obtain $I_0(\lambda, 0^-)$ the sea surface albedo was calculated following Sikorski and Zika (2012). To apply for the equations, direct and diffuse spectral incident irradiance was obtained by the Bird model (Bird and

Hulstrom, 1981):

$$f_{\text{abs}} = f_{\text{dir}}[(1.03 - A_{\text{dir}})(1 - f_{\text{ice}}) + f_{\text{ice}}] + f_{\text{dif}}[(1.03 - A_{\text{dif}})(1 - f_{\text{ice}}) + f_{\text{ice}}], \quad (6)$$

$$A = 1 - f_{\text{abs}}, \quad (7)$$

where f and A represent the fraction and albedo, and the subscripts, abs, dir, and dif, indicate absorption of sunlight as well as the direct and diffuse spectral incident irradiance, respectively. Then, we obtained the normalized irradiance as follows:

$$I(\lambda, 0^-) = I(\lambda, 0^+) \times (1 - A), \quad (8)$$

$$I_0(\lambda, 0^-) = I(\lambda, 0^-) \times \frac{I_{\text{obs}}}{I(\lambda, 0^+)}, \quad (9)$$

where $I(\lambda, 0^+)$ indicates the irradiance calculated by the TUV model, and $I_0(\lambda, 0^-)$ and $I(\lambda, 0^-)$ represent irradiance beneath the air–sea interface with and without normalization using the observed irradiance, I_{obs} .

The diffuse attenuation coefficient, $k_d(\lambda, z)$, was determined by following the algorithm in Sikorski and Zika (2012). It takes into account not only the absorption and scattering coefficients of seawater and particles, including phytoplankton, but also the reflectance of direct and diffuse spectral radiation in the water column (see Sect. S1 and Figs. S2 and S3 for details). Not measuring the apparent quantum yield (Φ_{CO}), we applied the parameterizations determined by Zafiriou et al. (2003) in order to determine the photochemical production rate (J).

2.7.2 Microbial oxidation

The microbial oxidation rate (M) was determined using first-order reaction kinetics involving the product of dissolved CO concentration (C_w), k_{CO} , and h :

$$M = k_{\text{CO}} \times C_w \times h. \quad (10)$$

In cases where an incubation experiment was not conducted, the mean value of k_{CO} was derived either within the specific geographic province or by averaging the values at the transition stations crossing the boundary of the provinces.

2.7.3 Air–sea flux

Based on the underway observations of CO in the surface seawater (C_w) and the overlying air (C_a), we calculated the air–sea CO flux (F) using the following equation:

$$F = k_w \times (C_w - LC_a), \quad (11)$$

where k_w and L represent the gas transfer velocity (in m s^{-1}) and the Ostwald coefficient of solubility, respectively. k_w is a function of wind speed and the Schmidt number (Sc). L was calculated using the definition described in Sect. 2.3.

We employed three different parameterizations of k_w (Table 1): Wanninkhof (1992) (W92), Nightingale et al. (2000) (N00), and Wanninkhof (2014) (W14). Ho et al. (2011) compiled the entire dual-tracer experiments to accurately parameterize the gas transfer velocity and found their parameterization to be virtually identical to that of Nightingale et al. (2000) within the associated uncertainties. The Wanninkhof (1992) parameterization, widely used, may indicate the potential maximum contribution of air–sea flux to the CO budget.

Since all these parameterizations are originally based on an Sc of 600 (Nightingale et al., 2000) or 660 (Wanninkhof, 1992), which are for CO_2 at 20°C in freshwater or in seawater, we normalized Sc to account for CO at the in situ temperature and salinity:

$$k_w = k(Sc_{\text{CO}}/Sc)^{-1/2}, \quad (12)$$

where k is the parameterization of the CO_2 gas transfer velocity (in m s^{-1}) and Sc_{CO} represents the Schmidt number for CO. We derived a parameterization of Sc_{CO} as a function of both temperature and salinity, as its parameterization in the literature (e.g., Zafiriou et al., 2008) considers temperature only (see Sect. S2 and Figs. S4 and S5 for details).

2.7.4 Vertical diffusion

The vertical diffusion rate (V) was calculated as the product of vertical eddy diffusivity (K_z ; in $\text{m}^2 \text{s}^{-1}$) and the vertical gradient of CO at the bottom of the mixed layer. K_z was obtained from a one-dimensional general ocean turbulence model (GOTM) that was forced by ECMWF reanalysis data (ERA5) and relaxed toward observed temperature and salinity vertical profiles at each station.

2.8 Statistical analysis

For statistical calculations, we utilized Microsoft Excel, Python, or IDL (Interactive Data Language, NV5 Geospatial) depending on the specific requirements. For instance, when estimating linear and exponential curve fitting to explore the relationships between parameters, we employed Python programming. The determination of k_{CO} values and error ranges, as well as the CO budget calculations, were carried out using the IDL program.

3 Results and discussion

3.1 Oceanographic settings of the provinces

3.1.1 The East Sea (Sea of Japan)

The Tsushima Warm Current (TWC) dominates the upper water column in the southern part of the ES, carrying eddies along its main current as it flows out through Tsugaru Strait (Kim and Yoon, 1996; Isobe, 2002). Despite originating from

Table 1. Summary of the observed parameters in the different provinces. Data are presented as the average and standard deviation (1σ), with the number of measurements or samples indicated in parentheses.

Properties (units)	East Sea (Sea of Japan)	North Pacific	Bering Sea
Air temperature ($^{\circ}\text{C}$)	20.5 ± 1.3 ($N = 85$)	12.0 ± 2.8 ($N = 140$)	7.7 ± 0.5 ($N = 91$)
Air pressure (hPa)	1008.5 ± 3.9 ($N = 85$)	1006.4 ± 4.4 ($N = 140$)	1004.5 ± 4.2 ($N = 91$)
Relative humidity (%)	84 ± 8 ($N = 85$)	92 ± 3 ($N = 140$)	92 ± 4 ($N = 91$)
U_{10N}^a (m s^{-2})	6 ± 4 ($N = 4791$)	9 ± 2 ($N = 10151$)	8 ± 2 ($N = 4663$)
Irradiance ($\text{MJ m}^{-2} \text{d}^{-1}$)	27.0 ± 0.4 ($N = 283$)	11.8 ± 3.4 ($N = 1024$)	8.9 ± 4.6 ($N = 428$)
SST ^b ($^{\circ}\text{C}$)	21.3 ± 1.9 ($N = 4755$)	11.8 ± 3.0 ($N = 10152$)	8.3 ± 0.3 ($N = 4662$)
SSS ^b (psu)	32.8 ± 1.2 ($N = 4755$)	32.9 ± 0.3 ($N = 10152$)	31.9 ± 1.0 ($N = 4662$)
Chl- <i>a</i> (mg m^{-3})	0.7 ± 0.4 ($N = 4752$)	0.9 ± 0.3 ($N = 10152$)	0.7 ± 0.4 ($N = 4663$)
MLD ^b (m)	11.4 ± 0.15 ($N = 2$)	13.7 ± 4.3 ($N = 6$)	12.7 ± 3.7 ($N = 2$)
$a_c(412)^c$ (m^{-1})	0.21 ($N = 1$)	0.16 ± 0.16 ($N = 6$)	0.17 ($N = 1$)
k_{CO}^c (h^{-1})	0.27 ± 0.05 ($N = 2$)	0.13 ± 0.15 ($N = 4$)	0.36 ± 0.39 ($N = 2$)
$[\text{CO}]_{\text{sea}}$ (nM)	0.5 ± 0.4 ($N = 80$)	0.6 ± 0.4 ($N = 140$)	1.6 ± 1.3 ($N = 91$)
CO_{air} (nmol mol^{-1})	141 ± 38 ($N = 85$)	112 ± 29 ($N = 99$)	102 ± 10 ($N = 74$)
SA ^b	3.1 ± 2.7 ($N = 80$)	5.0 ± 4.4 ($N = 99$)	14.3 ± 13.8 ($N = 74$)
Air–sea CO flux ($\mu\text{mol m}^{-2} \text{d}^{-1}$)	W92 ^d	0.8 ± 0.9 ($N = 80$)	2.2 ± 3.0 ($N = 99$)
	N00 ^e	0.7 ± 0.8 ($N = 80$)	1.7 ± 2.3 ($N = 99$)
	W14 ^f	0.6 ± 0.8 ($N = 80$)	1.7 ± 2.4 ($N = 99$)

^a Neutral wind speed at 10 m high. ^b SST, SSS, MLD, and SA stand for sea surface temperature, sea surface salinity, mixed layer depth, and saturation anomaly, respectively. ^c $a_c(412)$ and k_{CO} designate the absorption coefficient of CDOM at the wavelength of 412 nm and the microbial oxidation constant, respectively. ^{d,e,f} Gas transfer velocity parameterizations by Wanninkhof (1992), Nightingale et al. (2000), and Wanninkhof (2014), respectively.

the Kuroshio Current, which transports salt and heat from the western part of the Equator and branches in the southwestern part of the Japanese archipelago, the physical properties of the TWC undergo slight modifications in the East China Sea due to mixing with freshwater flowing from Yangtze River (Morimoto et al., 2009; Isobe, 2002).

The highest SST of 22.4°C and SSS of 34 were registered in the ES, indicating the dominant influence of TWC on the surface waters (Fig. 2f). The southern part of the ES often experiences the development of warm eddies due to the meandering of TWC horizontally (Isoda and Saitoh, 1993), characterized by high salinity and warm water in the Ulleung Basin near station 1 and Yamato Rise around station 2. On the other hand, the North Korea Cold Current flows southwards from near Vladivostok along the east coast of the Korean Peninsula, and on 15 July, it was detected with temperature 1°C lower (22.5°C) and salinity 2–3 units lower (< 32) than TWC. As TWC approaches the Tsugaru Strait in the ES, there is a slight, decreasing tendency in SST from ~ 22 to $\sim 20^{\circ}\text{C}$ and an increasing tendency in SSS from 33.5 to 33.8. This is due likely to higher latitude of the Tsugaru Strait than in the inlet of TWC, the Korea Strait, as well as the branching and meandering of TWC in the ES. Upon entering the mouth of the Tsugaru Strait, the SST dropped by 4°C from $\sim 21.5^{\circ}\text{C}$, despite a nearly constant or slight decrease in SSS by ~ 0.5 , pointing to the sudden change in the water mass crossing the strait, likely influenced by the Oyashio currents from the North Pacific (Yasuda, 2003).

Due to the oligotrophic characteristics of the TWC (Kwak et al., 2013), Chl-*a* concentration in the surface along the ship track were lower than 0.5 mg m^{-3} except for the coastal area near the Korean Peninsula (Fig. 2g). MLDs at stations 1 and 2 were nearly 11 m (Table 1).

3.1.2 The North Pacific

The NP province is governed by the Western Subarctic Gyre (WSAG), which is operated by both its western boundary currents and the Subarctic Current. The former is composed of the East Kamchatka and the Oyashio currents, flowing southward along the Kamchatka Peninsula, Kuril Islands, and Hokkaido southward (Yasuda, 1997), while the latter returns to the northeast and merges into the Kuroshio Extension (Yasuda, 2003). The Subarctic Current is bounded by, and mixes with, the Kuroshio Extension, forming the Subarctic Front southward into the WSAG. This front extends from the Kuroshio–Oyashio confluence region off Hokkaido, where the Kuroshio Extension and the Oyashio Current intermingle.

Upon leaving the Tsugaru Strait, the SST remained nearly constant at 16 – 17°C , while the SSS fluctuated between 32.5 and 33.5, indicating the mixing of the weak Oyashio Current and the strong Kuroshio Extension offshore of Hokkaido, where the Kuroshio–Oyashio confluence region is located and the Subarctic Current forms along the Subarctic Front (Yasuda, 1997). This Subarctic Front covers stations 3 and 4 until 154.6°E , in front of Kuril Islands, where the SST

and SSS suddenly decreased by 6 °C from 16.5 °C and by 1 unit from 33.6, respectively, indicating entry into the WSAG (Figs. 1 and 2) (Yasuda, 1997). In the WSAG, the SST and SSS remained almost constant at 9 °C and 32.8, respectively. Approaching station 8, the SST and SSS slightly increased by ~ 1 °C and 0.2 units, respectively, alluding to the crossing of a warm core ring. As the WSAG crosses the Aleutian Islands (Kuroda et al., 2021), we extended the NP province to station 9.

The WSAG is known as a high-nutrient low-chlorophyll (HNLC) region where primary production is believed to be limited by the availability of dissolved iron (Fujiki et al., 2014). This is reflected in the higher variability (0.2 mg m^{-3}) and mean value of Chl-*a* concentration (0.9 mg m^{-3}) in the NP compared with the marginal seas, i.e., the ES and BS (Fig. 2g; Table 1). The MLD at the NP stations ranges from 10 to 12 m, except for stations 5 and 9 where the MLDs were 18 and 21 m, respectively. Excluding these two stations, the mean MLD was similar to that in the ES, but it would deepen to 14 m if both stations were included.

3.1.3 The Bering Sea

The Bering Sea is a marginal sea separated from the North Pacific by the Commander and Aleutian islands. Despite this geographical separation, the influence of the WSAG extends into the Bering Basin, primarily through the Kamchatka and Nier straits. It circulates cyclonically along Bowers and Shirshov ridges, eventually returning to the North Pacific via the Kamchatka Strait, carried by the Kamchatka Current (Stabeno et al., 1999). Therefore, we extended the North Pacific province to include station 9 (Fig. 2).

Upon crossing longitude 176.4° E on 25 July, we observed a slight increase in salinity, and the dissolved CO concentration suddenly soared, suggesting the influence of other water masses. Indeed, the Alaskan Stream flows westward from the Alaska Gyre, entering the Bering Basin through the Nier Strait and various Aleutian passes, particularly Amchitka Pass. It then veers cyclonically along the Bering Slope toward the Kamchatka Peninsula, forming the Kamchatka Current (Stabeno and Reed, 1994). After leaving station 10, salinity fell from 32.6 to 29.9 in just 8 h, indicating the encounter with different water masses.

The inner shelf of the BS is dominated by the Alaska Coastal Current, which delivers fresh, low-nutrient water to the BS, primarily through the Unimak Pass, and ultimately reaches the Beaufort Sea in the Arctic through the Bering Strait (Yamamoto-Kawai et al., 2006; Ladd and Stabeno, 2009). The significant variation in the SSS observed on the inner shelf of the BS indicates a heterogeneous spatial distribution and relatively short residence time of the Alaska Current before entering the Bering Strait. At station 12, located near the Bering Strait, the SST and SSS significantly differed from those observed on the inner shelf. Salinity reached values observed in the outer shelf, but the exceptionally low

temperature, around 1 °C, suggests the influence of water mass originating from the Gulf of Anadyr.

Chl-*a* concentration in the surface waters of the BS was lower than that in the NP, but similar to that in the ES, with a mean value of 0.7 mg m^{-3} . However, it significantly increased to over 8 mg m^{-3} near the Alaska coast at station 12, likely due to the inflow of nutrients from the Gulf of Anadyr. The MLD at the station in the Bering Basin was 16 m, while it shoals to ~ 11 m at the stations in the continental shelf.

3.2 Atmospheric situations

Air temperature and pressure, as well as daily insolation, generally decrease with increasing latitude (Table 1). Following the SST, the air temperature was as high as 25 °C in the Ulleung Basin of the ES and gradually decreased to 16 °C until R/V *Araon* passed the Tsugaru Strait. Upon leaving the strait, the air temperature dropped by 7 °C and then continued to decrease slowly to 10 °C in front of Nome. Air pressure was high in the ES (1008 hPa) and low in the NP (1006 hPa) and the BS (1005 hPa). This pressure gradient along the ship track is reflected in the insolation, with cloudy or overcast conditions in the NP and BS, and sunny conditions in the ES, where the irradiance was more than twice that in the NP and BS (Fig. 2c). Wind speed showed an opposite trend to air pressure and insolation, with the mean U_{10N} in the ES being 6.2 m s^{-1} , approximately two-thirds of that in the NP and BS.

3.3 CO in the surface mixed layer and overlying air

During the expedition, we measured the mole fraction of CO in the atmosphere using two different analytical systems. An automated analysis system measured the CO mole fractions in the surface mixed layer of the ocean and the overlying air. Additionally, we used an off-axis integrated cavity output spectroscope (Off-Axis ICOS: N₂O / CO analyzer; Los Gatos Research) to observe highly resolved variability in CO within the surface marine boundary layer (Park and Rhee, 2015). The mean absolute difference in atmospheric CO mole fractions between the two analytical techniques was only $3.2 \text{ nmol mol}^{-1}$ for this campaign, demonstrating that our measurements were in reasonable agreement (see Fig. S1 in Park and Rhee, 2015). Furthermore, we confirmed the consistency of our measurements with values obtained at the NOAA/ESRL global network stations (<https://gml.noaa.gov/>, last access: 15 October 2015) located near our cruise track or within the same latitudinal zone within a 3–5 d time window to our onboard observations (Fig. 2a). Atmospheric CO mole fractions displayed significant variability, with approximately a 30 % variation relative to the mean value of $118 \text{ nmol mol}^{-1}$. This variability is associated with various sources, including anthropogenic emissions in the Northern Hemisphere, particularly on the Chinese mainland and the Korean Peninsula as discussed in Park and Rhee (2015). Ad-

ditionally, the decreasing trend in provincial mean values appears to be influenced by factors such as distance from anthropogenic source areas and, in the northern sections, contributions from wildfires in East Siberia.

The diurnal variation of dissolved CO concentrations ([CO]) in surface waters exhibits a marked fluctuation following solar irradiance, indicating that photochemical CO production is the main driver (Conrad et al., 1982; Ohta, 1997; Zafiriou et al., 2008). However, this typical diurnal oscillation disappears in the area around the Aleutian archipelago, due probably to overcast conditions along the cruise track (Fig. 2c), and in the Bering Sea, with decreasing solar irradiance. Except for 25 and 26 July, daily minimum values range from 0.04 to 0.63 nmol kg⁻¹, and maximum values range from 0.47 to 2.09 nmol kg⁻¹, respectively. Along the cruise track, the minimum and maximum dissolved [CO] were 0.04 and 4.6 nmol kg⁻¹, respectively, varying over 100 % with respect to an average of 0.8 (±0.9) nmol kg⁻¹. The maximum value appeared in the central Bering Sea on 25 July.

Our mean value is slightly lower than or comparable to the Pacific mean value, 1.0 nmol kg⁻¹ (Bates et al., 1995), the mean observed in the Sargasso Sea, 1.1 ± 0.5 nmol kg⁻¹ (Zafiriou et al., 2008), and the mean at the tropical south Pacific station, approximately 1 nmol kg⁻¹ (Johnson and Bates, 1996). It is important to note that our study area, along with the mentioned regions, all falls under the category of Case 1 waters, where the Chl-*a* concentration can serve as a proxy for CDOM production, as discussed in Steinberg et al. (2004). Therefore, the combination of low productivity and overcast conditions can partially explain our lower mean CO concentration (Fig. 2c and g).

3.4 Spectral CDOM absorbance

The optical properties of CDOM can be characterized by its absorption coefficient at a reference wavelength, λ_0 (= 412 nm), denoted as $a_c(\lambda_0)$, and its slope (S) as defined in Eq. (3) (Bricaud et al., 1981). $a_c(\lambda_0)$ reflects the CDOM content in seawater, while S indicates either the source of CDOM or its degradation process. The spectral profile of $a_c(\lambda)$ in surface seawater decreases exponentially with increasing wavelength (Fig. 3a). Fitting the raw data into Eq. (3) reveals that the $a_c(412)$ ranged from 0.031 m⁻¹ (station 9) to 0.26 m⁻¹ (station 4). In Fig. 3b, logarithmic values of $a_c(412)$ are inversely correlated with S over the 350–600 nm wavelength range. This inverse relationship is consistent with the observations in the Atlantic Ocean.

The values of $a_c(\lambda)$ at the measured wavelengths showed clear separation into two groups: a marginal sea group in the ES (station 1) and the BS (station 11), and an open-sea group in the NP (stations 5–9). Although stations 3 and 4 belong to the NP province, the spectra of $a_c(\lambda)$ at these stations are quite different from those observed at stations 5–9. Instead, they are similar to those in the ES and the BS.

This suggests that the composition of CDOM at stations 3 and 4 should be influenced by the continental sources (e.g., Vodacek et al., 1997) by means of the Kuroshio Current flowing northward along the Japanese east coast and of the Oyashio Current which meanders in the Okhotsk Sea. As mentioned earlier, the surface waters at stations 3 and 4 are located in the Kuroshio–Oyashio confluence zone as their mean SST (= 15.5 ± 0.5 °C) and SSS (= 33.0 ± 0.4) were higher than those for stations 5–9 by 6.1 °C and 0.25, respectively (Fig. 2f). The $a_c(\lambda)$ spectra are consistent with this physical setting of stations 3 and 4 (Yamashita et al., 2010; Takao et al., 2014).

3.5 Microbial CO consumption rate constants

Figure 4a–c shows the results from the dark incubation experiments carried out on board. Despite our careful experiments, we did not observe a reduction in dissolved [CO] over time due to microbial oxidation, as would be expected. This could be attributed to various factors, such as an inadequate blank correction, the existence of a threshold [CO] for consumption (Xie et al., 2005), or the possibility of dark production of CO (Zhang et al., 2008). Nonetheless, we applied a first-order decay function to extract the main trend of CO oxidation, despite the considerable errors caused by the scattered data.

The k_{CO} in the surface mixed layer exhibited significant variability, ranging from 0.001 to 0.465 h⁻¹, with an average of 0.22 ± 0.13 h⁻¹ (Fig. 4d). The minimum and maximum k_{CO} values were obtained at station 9 in the NP and at station 11 in the BS, respectively. Mean k_{CO} values in the ES, NP, and BS were determined to be 0.27(±0.05) h⁻¹, 0.13(±0.15) h⁻¹, and 0.36(±0.39) h⁻¹, respectively. The decrease in the mean k_{CO} values from the marginal seas to the open oceans aligns with previous findings compiled by Xie et al. (2005), indicating a decreasing trend in k_{CO} from bay to offshore areas. Xie et al. (2005) speculated that the high k_{CO} observed in the Beaufort Sea in their study might be due to the Arctic Ocean receiving substantial inputs of terrestrial organic carbon which promote the growth of microbial communities. Indeed, considerable fluvial input of organic carbon has been observed over the Bering Sea near the Arctic Ocean (Walvoord and Striegl, 2007; Mathis et al., 2005). This could partially explain the higher k_{CO} in the Bering Sea compared with the East Sea, despite both being marginal seas. Nonetheless, as Fig. 4d shows, the mean k_{CO} values in the marginal seas (the ES and BS) and at station 4 in the NP are larger than the values measured in the NP, alluding to a division of microbial activities between terrestrial and open-ocean influences. As indicated by the absorption spectrum of the CDOM, the MLD water masses at station 4 should be affected by the terrestrial input.

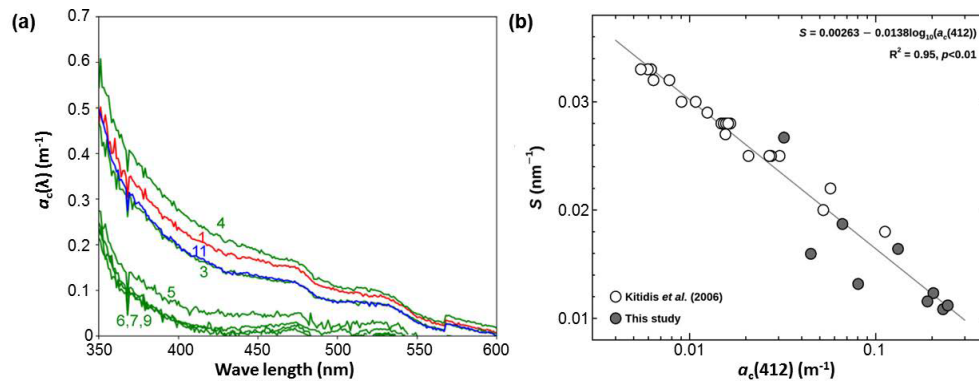


Figure 3. Panel (a) shows the spectra of the CDOM absorption coefficient ($a_c(\lambda)$) in the surface seawater at the given stations and (b) is a semi-log scatter plot between the spectral slope (S) and the absorption coefficient at the reference wavelength of 412 nm ($a_c(412)$). Numbers in (a) indicate hydrographic stations.

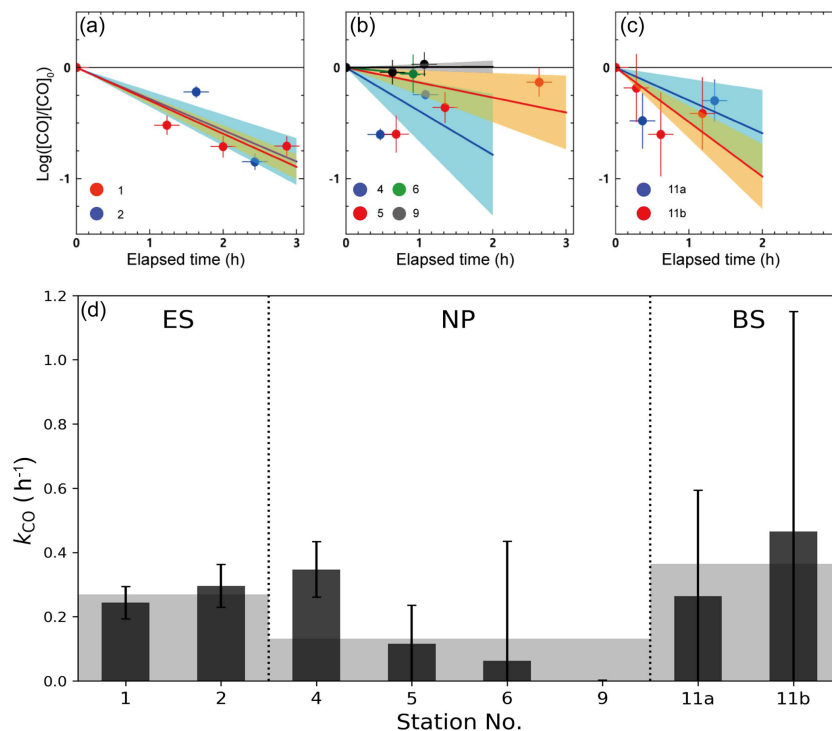


Figure 4. Temporal variation of the dark incubation experiment conducted at the stations in (a) the ES, (b) the NP, and (c) the BS, as well as (d) microbial oxidation rate coefficients (k_{CO}) obtained from the dark incubation experiments. Solid lines and shading in (a)–(c) denote the linear fits and their uncertainties, respectively, and gray shading in (d) indicates the mean values of k_{CO} in the given provinces.

3.6 CO budget in the mixed layer

3.6.1 Photochemical production

The photochemical production rate (J) would typically decrease with increasing latitude if it were solely dependent on the daily integrated insolation (Fig. 5; Table 1). However, the provincial mean J value in the ES was approximately twice larger than that in the NP and BS. There was little difference between the NP and BS, despite the lower insolation

in the BS. This anomaly can be attributed to the high content of CDOM in the BS (Fig. 3a; Table 1). The elevated J value in the ES can be attributed to the combined effect of both high insolation and a significant CDOM presence in the surface seawater. At stations 3 and 4, the reduced insolation was somewhat compensated for by the high CDOM content (Fig. 3a), resulting in a J value similar to that at the other stations in the NP.

The photochemical production rate of $56 \mu\text{mol m}^{-2} \text{d}^{-1}$ in the ES is comparable to those reported in oligotrophic

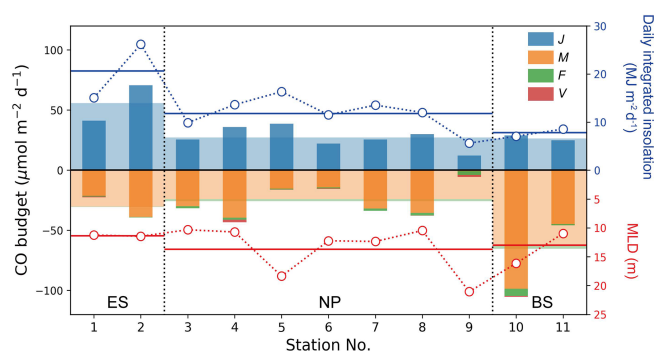


Figure 5. CO budget terms in the mixed layer at each station. Daily photochemical production (J), microbial oxidation (M), air–sea gas exchange (F), and vertical mixing (V) are denoted by blue, orange, green, and red bars, respectively. Wide, transparent bars represent the mean values for these processes in the given provinces. Daily-integrated insolation and MLD are represented by respective open blue and red circles with dotted line, and solid horizontal blue and red lines indicate their mean values in the provinces.

regions, e.g., 68 and $52 \mu\text{mol m}^{-2} \text{d}^{-1}$ in spring and August, respectively, in the Bermuda Atlantic Time-series Study (BATS) (Zafiriou et al., 2008), and 56 and $83 \mu\text{mol m}^{-2} \text{d}^{-1}$ at South Pacific Gyre (SPG) and the Pacific equatorial upwelling (PEU) zone, respectively (Johnson and Bates, 1996). On the other hand, the J values in the NP and BS ($\sim 30 \mu\text{mol m}^{-2} \text{d}^{-1}$) are lower due to declining insolation with latitude and lower CDOM content in the NP, as mentioned above (Fig. 3a; Table 1).

3.6.2 Microbial oxidation

The microbial oxidation rates were higher in the marginal seas of the ES and BS, which is attributed to the high k_{CO} in those two provinces, despite the relatively low mean dissolved $[\text{CO}]$ in the ES (Tables 1 and 2). Station 10 had the highest microbial oxidation rate of $99 \mu\text{mol m}^{-2} \text{d}^{-1}$, while station 9 showed the lowest value of $0.8 \mu\text{mol m}^{-2} \text{d}^{-1}$. This result is due to the high k_{CO} and exceptionally high surface $[\text{CO}]$ near station 10 (Fig. 2b). By leaving aside station 9, the M values range an order of magnitude with the second lowest value of $14.4 \mu\text{mol m}^{-2} \text{d}^{-1}$ at station 6, and it does not show any dependence on latitude. Compared with microbial oxidation rates obtained at BATS, SPG, and PEU that ranged from 22 to $45 \mu\text{mol m}^{-2} \text{d}^{-1}$ (Zafiriou et al., 2008; Johnson and Bates, 1996), the high mean value in the BS can be attributed to the distinct microbial community structure or biomass of CO-oxidizing species.

3.6.3 Air–sea flux

The air–sea CO flux (F) depends on both, the $[\text{CO}]$ difference between the surface seawater and the overlying air, and gas transfer velocity mainly driven by wind speed (see Eq. 11). The former is sometimes transformed to a satura-

tion anomaly ($\text{SA} = \frac{C_w}{C_a} - 1$; Fig. 2b) which directly indicates whether the ocean is a source or sink for atmospheric CO. Throughout the campaign, most of the dissolved CO remained supersaturated, spanning over two orders of magnitude in SA, e.g., -0.6 – 51 , resulting in outgassing of CO from the ocean to the atmosphere. The mean SAs in provinces increase with latitude due to an increase in dissolved $[\text{CO}]$ and, in part, to a decrease in atmospheric CO concentration (Table 1).

The air–sea CO flux densities ranged from -0.5 to $19 \mu\text{mol m}^{-2} \text{d}^{-1}$ (Fig. 2e), resulting in an average of $2.0 (\pm 3.6) \mu\text{mol m}^{-2} \text{d}^{-1}$ over the cruise track. The mean F values of the provinces are, however, quite different, with the lowest value in the ES ($0.4 \mu\text{mol m}^{-2} \text{d}^{-1}$) and the highest in the BS ($2.7 \mu\text{mol m}^{-2} \text{d}^{-1}$). In the NP, the air–sea flux ($1.7 \mu\text{mol m}^{-2} \text{d}^{-1}$) is comparable to those observed in the open ocean: $2.2 (\pm 1.5)$ and $2.7 (\pm 1.9) \mu\text{mol m}^{-2} \text{d}^{-1}$ in the North and South Atlantic, respectively (Park and Rhee, 2016); $2.93 (\pm 2.11) \mu\text{mol m}^{-2} \text{d}^{-1}$ in the oligotrophic Atlantic Ocean (Zafiriou et al., 2008); $2.7 \mu\text{mol m}^{-2} \text{d}^{-1}$ in the oligotrophic equatorial Pacific Ocean (Johnson and Bates, 1996); and $1.94 \mu\text{mol m}^{-2} \text{d}^{-1}$ in the NP between 30 and 45°N in summer (Bates et al., 1995). On the other hand, both marginal seas, the ES and BS, show stark differences in air–sea flux: that in the ES is even lower than in the NP due to higher atmospheric CO concentration and weaker wind speed in the ES. However, in the BS dissolved $[\text{CO}]$ was the highest among the three provinces and the wind was strong. Even the air–sea fluxes observed near the Bering continental slope on 25 July were orders of magnitude higher than those of any other expedition period. Such a high outgassing rate has been reported in the productive regions, e.g., $22.8 \mu\text{mol m}^{-2} \text{d}^{-1}$ in the central Pacific (Johnson and Bates, 1996), 4.6 – $9.6 \mu\text{mol m}^{-2} \text{d}^{-1}$ in the Mauritanian upwelling (Kitidis et al., 2011), and $5 \mu\text{mol m}^{-2} \text{d}^{-1}$ in the northern California upwelling (Day and Faloon, 2009). Compared with the microbial oxidation (M), the outgassing by air–sea gas exchange plays a minor role as a sink: their fractions in the sink strength are merely from 1.3 % in the ES to 6.4 % in the NP (Table 2).

3.6.4 Vertical diffusion

The vertical diffusion rate (V) relies on the eddy diffusivity and the gradient of dissolved CO concentration at the bottom of the mixed layer. Most of the daily mean eddy diffusivities range from $8 \times 10^{-5} \text{m}^2 \text{s}^{-1}$ (station 11) to $37 \times 10^{-5} \text{m}^2 \text{s}^{-1}$ (station 6), while notably high values were estimated at stations 2 ($74 \times 10^{-5} \text{m}^2 \text{s}^{-1}$) and 10 ($120 \times 10^{-5} \text{m}^2 \text{s}^{-1}$). The vertical diffusion rate of dissolved CO at the bottom of the mixed layer was $0.6 \mu\text{mol m}^{-2} \text{d}^{-1}$ on average, with the exception at station 2 where V acted as a source of $0.1 \mu\text{mol m}^{-2} \text{d}^{-1}$ (Fig. 5). The V term accounts for approximately 34 % of the gas exchange rate and only 2 % of the photochemical production of CO on average, demonstrating

Table 2. Daily mean CO budget (in $\mu\text{mol m}^{-2} \text{d}^{-1}$) in the mixed layer of the given provinces based on the observations at the hydrographic stations. Uncertainties indicate standard errors ($= 1\sigma/\sqrt{n}$).

Province	Photochemical production (J)	Microbial oxidation (M)	Air–sea flux (F)	Vertical diffusion (V)
East Sea (Sea of Japan)	56 ± 15	30 ± 8	0.4 ± 0.1	0.3 ± 0.4
North Pacific	27 ± 3	24 ± 5	1.7 ± 0.3	0.7 ± 0.4
Bering Sea	26 ± 2	63 ± 19	2.7 ± 1.7	0.3 ± 0.2

that the vertical diffusion is negligible for the marine CO cycle, as noted by Zafiriou et al. (2008).

3.6.5 CO budget imbalances

According to a simple budget calculation by Eq. (4), we estimated the CO budget in the surface mixed layer at each station (Fig. 5). The CO budget was balanced in the open ocean, the NP, but not in the marginal seas, the ES and BS. However, it is important to note that the large uncertainties in the budget terms leave room for potential balance. The CO cycle in the ES was dominated by photochemical production, which was approximately twice as large as the entire sink strengths, while strong microbial oxidation in the BS resulted in a net sink in the mixed layer of $\sim 60 \mu\text{mol m}^{-2} \text{d}^{-1}$, which is approximately twice larger than the photochemical production. Although the uncertainties in budget terms in the ES and BS are fairly large, their mean values suggest that the CO cycles in the ES and BS require external CO transport in the water column to stay in steady state during the observation period.

3.7 Vertical distribution and column burden of CO

In general, [CO] exponentially decreases with depth in the water column due to limited penetration of short-wavelength radiation that effectively stimulates CO production (Conrad et al., 1982; Johnson and Bates, 1996; Kettle, 2005b; Zafiriou et al., 2008). This typical depth-profile pattern was observed at the stations in the NP, while the vertical [CO] profiles at stations in the BS showed very low concentrations in MLD ($\sim 0.6 \text{ nM}$). In the ES, [CO] remained around 1 nM even at the aphotic deep water without any vertical gradients (Fig. 6a, b, and c). Excluding stations 1 and 2, the minimum and maximum CO concentrations in MLD were $0.80(\pm 0.19) \text{ nmol kg}^{-1}$ (station 10) and $3.32(\pm 0.23) \text{ nmol kg}^{-1}$ (station 3), respectively, and the mean value was $1.83 \text{ nmol kg}^{-1}$. At depths deeper than 200 m, the CO concentrations converge toward the value less than that of the detection limit ($< 0.1 \text{ nmol kg}^{-1}$).

Surface CO concentrations at some stations in the ES and NP appear to differ from the values observed underway (see Fig. 2b). This discrepancy can be attributed to the significant horizontal and vertical variabilities in CO concentrations driven by the rapid photochemical production and microbial oxidation evidenced by the strong diurnal cycle and the expo-

ponential decrease with depth (e.g., Zafiriou et al., 2008). This diurnal variation is more pronounced at lower latitudes than at higher latitudes (Fig. 2b). The latitudinal attenuation of the diurnal amplitude trend is evident in the degree to which dissolved CO concentrations exponentially decrease with depth (see Fig. 6a, b, and c).

We assessed the impact of this vertical gradient of the CO to the difference in CO concentration between underway and discrete measurements (Fig. S6). Given the coarse resolution of the CO profiles, we first applied curve fitting to the profile and estimated the vertical gradient of dissolved CO at the depth at which the seawater was continuously supplied for the underway observation of surface CO concentrations. As illustrated in Fig. S6, a greater vertical gradient at the depth of the seawater inlet to the underway system corresponds to a larger difference in CO concentrations between the underway observation and discrete measurement. In addition to the vertical gradient, horizontal variability likely plays a role in the difference of the CO concentrations between the two methods (Wanninkhof and Thoning, 1993), as evidenced at stations 8 and 9 (Fig. 2b).

Another factor to consider when comparing surface CO concentrations using the two methods is that continuous observation in the underway system can mitigate the presence of high or low spikes in dissolved CO concentrations due to the long equilibration time associated with sparingly soluble gases, such as CO (Johnson, 1999). Considering these spatial variabilities in CO concentrations and the dynamic equilibration occurring in the underway system, it is possible to obtain different CO concentrations using the two sampling methods for measuring dissolved CO.

By integrating the observed vertical profile of CO over 200 m depth, we computed the column burden of CO at each station (CB_{200} ; Fig. 6a, b, c, and d). The mean CB_{200} values were $183.7(\pm 51.14) \mu\text{mol m}^{-2}$ in the ES, $66.0(\pm 27.1) \mu\text{mol m}^{-2}$ in the NP, and $13.2(\pm 1.2) \mu\text{mol m}^{-2}$ in the BS, drastically decreasing with latitude, contrary to the slight increase in the surface CO concentration ($[\text{CO}]_{\text{sea}}$) with the increasing latitude. Our CB_{200} values in the NP and BS are roughly similar to the values reported in oligotrophic areas. The CB_{200} from the BATS station was $95 \mu\text{mol m}^{-2}$ in March and $39 \mu\text{mol m}^{-2}$ in August (Zafiriou et al., 2008), and the CB_{200} within the SPG was $51 \mu\text{mol m}^{-2}$ in April (Johnson and Bates, 1996). In contrast, the large CB_{200} value in

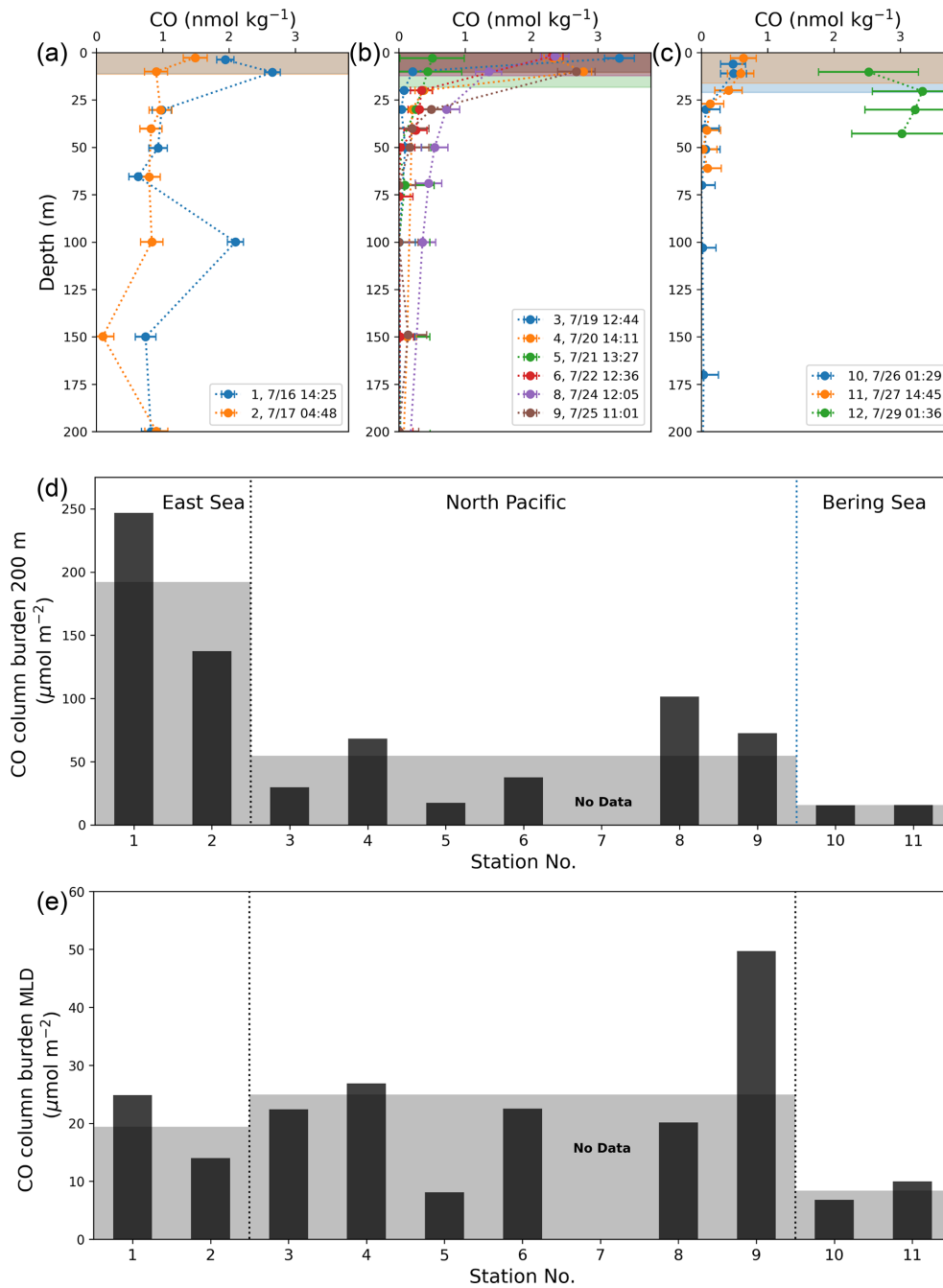


Figure 6. Vertical depth profiles of CO concentrations in the provinces of (a) the ES, (b) the NP, and (c) the BS, as well as (d) their column burdens of CO down to 200 m deep (CB₂₀₀) and (e) in MLD at the given stations. Shading in (a)–(e) indicates mixed layers at each station, and in (d) and (e) for the mean values of CB₂₀₀ and CB_{MLD} in each province.

the ES is of the same order of magnitude as the column burden in the productive PEU zone in December (283 μmol m⁻²; Johnson and Bates, 1996).

We also calculated the column burden of CO within the MLD (CB_{MLD}; Fig. 6e) at each station to examine whether the CO dynamics in MLD can be representative of those in the whole water column, accounting for the predominant

photochemical production of the CO in the surface mixed layer (Johnson and Bates, 1996), rather than homogeneous microbial oxidation in the water column (Kettle, 2005a; Gnanadesikan, 1996). Contrary to CB₂₀₀, the CB_{MLD} does not exhibit any consistent trend among the provinces.

3.8 Different trends between CB_{200} and CB_{MLD}

In this study, we calculated the CO budget within the MLD, the difference between the biogeochemical source and sink terms of CO, as well as the absolute total column burden of CO in the water column, based on observations of various parameters. Several key points can be summarized as follows: first, we found that the biogeochemical production and removal of CO are nearly balanced only in the NP, whereas in the BS, the sink term significantly outweighs the source term, resulting in an imbalance in the CO budget. Second, despite the CO budget values in the NP and BS being close to or below zero, there are no distinct differences in CB_{MLD} between the provinces, and no apparent relationship between CB_{MLD} and the CO budget in the mixed layer, as shown in Fig. 7a ($R^2 = 0.02$). Third, when considering the integrated CO down to a depth of 200 m (CB_{200}), we observed a significant correlation, indicating an increasing trend in the order of the BS, NP, and ES ($R^2 = 0.25$; Fig. 7b). This finding may seem counterintuitive as the relative magnitude of the column burden should not change with the integration depth below the MLD. This is based on the assumption that vertical turbulence diffusion has a minimal impact on the CO cycle (see Table 2), and photochemical CO production predominantly occurs in the euphotic zone within the MLD. To interpret these results, we cautiously propose the importance of the three-dimensional physical supply processes of CO based on the observed vertical distribution of the CO.

3.9 Implications for potential missing processes

In the ES, the upper MLD of the water column accounted for approximately 10 % of the CB_{200} on average. This distribution reflects a relatively uniform concentration of CO regardless of depth. In contrast, in the NP and BS, the upper MLD accounted for approximately 51 % and 53 % of the CB_{200} , respectively, indicating a more concentrated distribution within the surface layer. The unique vertical distribution of CO in the ES, characterized by minimal variation with depth, is clearly evident in Fig. 5. While the highest concentrations are observed within the surface MLD, CO levels remain relatively high even at depths below the MLD, where concentrations should ideally fall below the detection limit. The relatively uniform distribution of high CO concentrations at the ES stations can be attributed to the subduction of surface water with elevated CO levels, as there is no significant penetration of irradiance to depths greater than 100 m, nor is there vigorous vertical mixing capable of overwhelming microbial oxidation observed in the ES province (see Fig. S3c and d). We hypothesize that the subduction of surface water is driven by warm core eddies, such as the Ulleung Warm Eddy (UWE), which is derived from the warm core of its subsurface structure (Kim and Yoon, 1999) and originates from the East Korean Warm Current, a northward branch of the Tsushima Warm Current (Shin et al., 2005).

Given that several studies (Isoda and Saitoh, 1993; Capotondi et al., 2019; Ichiye and Takano, 1988) describe the eddies with the core temperature and salinity of 5–10 °C and 34.1–34.3 near 200 m depth, station 1 appears to be located at the edge of a warm core eddy (Fig. S7a and b). This unique feature of a dynamic eddying flow field that subducts surface water with high concentrations of organic carbon and dissolved oxygen has also been observed in the North Atlantic Ocean (Omand et al., 2015).

In contrast, the behavior of CO in the BS province appears to be influenced by lateral transports, unlike ES, where subduction of high-CO surface water might be responsible. In this area, [CO] remained above ~ 0.5 nM in the upper layers (Fig. 6c), although the total sink strengths were much higher than the source strength. Moreover, a significant peak in surface [CO] was observed around station 10 (Fig. 2b) despite the small column burden of the BS. These observations imply that the CO inventory in the water column cannot be fully explained only by the biogeochemical processes with the Eulerian approach. Station 10 is located at the eastern boundary of the Aleutian Basin where the bottom depth is drastically altered (Figs. 1 and 2f). The Bering Slope Current (BSC; Kinder et al., 1975) flows northwestwards along the slope passing through this station. At around 54° N, 167° W where the BSC starts, the Alaska Current (AC), which has a high concentration of dissolved organic carbon (DOC) originating from Alaska coastal runoff, mixes with the BSC (Chen et al., 2009). According to D'Sa et al. (2014), the DOC concentrations are twice as high as the surrounding waters at this point. Given that the mean velocity of the BSC is about 34 km d^{-1} (Ladd and Stabeno, 2009), this water of high photochemical CO production from replete organic carbon may potentially influence the area of station 10. The sudden decrease in SSS right after passing through station 10 also implies potential freshwater contribution. Similarly, the column burden at station 11 is comparable to that of other stations despite the higher sink strengths than the source strength, which can be explained by the lateral flux of high CO surface waters from the coastal region. Station 12, located near station 11, is in the coastal area of Alaska (Fig. 1) and can be defined as an independent station not belonging to any provinces defined in this study. Aagaard et al. (2012) reported considerable horizontal shears and large lateral transports near station 12 in the Bering Strait. The strong horizontal velocities and shallowness of the water columns can lead to interaction between surface-forced and bottom-forced boundaries. We found that the water column of station 12 is relatively well mixed, as indicated by the CTD profiles of this station (Fig. S7j, k, and l). While the CB_{MLD} of station 12 shows a low value (Fig. 7a), the column burden over the total water column (~ 40 m) of the station shows a high value comparable to the values of the ES stations (Fig. 7b). Therefore, the high CO coastal water near station 12 can be considered a source for high column burden relative to the low production rate of station 11.

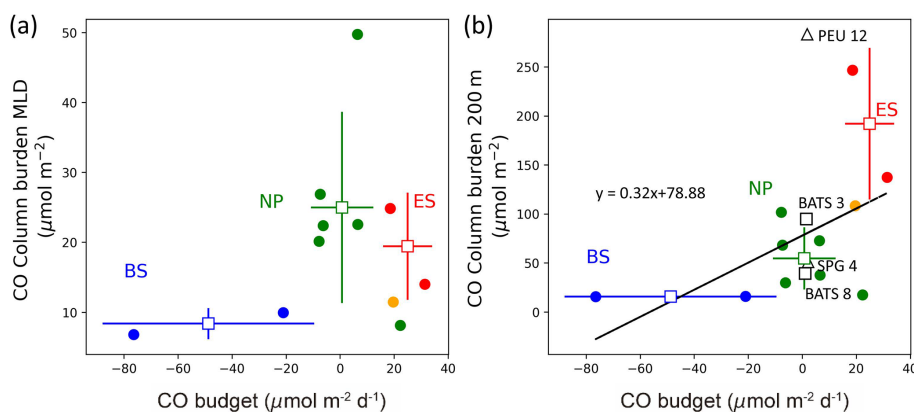


Figure 7. Comparison of CO column burdens **(a)** in the mixed layer (CBMLD) and **(b)** from the surface down to 200 m deep (CB200) against the CO budget in the mixed layer. In **(b)**, open black squares and triangles are from Zafiriou et al. (2008) and Johnson and Bates (1996), respectively, where BATS 3 and 8 refer to the Bermuda Atlantic Time-series Study in March and August, respectively, PEU 12 refers to the Pacific equatorial upwelling region in December, and SPG 4 refers to the South Pacific Gyre in April. The solid orange circle in **(a)** and **(b)** represents station 12 off the coast of Nome, Alaska.

Previous studies suggested that horizontal advection and lateral stirring across a front can drive much of the sub-mesoscale heterogeneity in $p\text{CO}_2$ (Mahadevan et al., 2004). Other recent studies have also shown that lateral transport can explain the observed distribution of methane (CH_4) and dimethyl sulfide (DMS) in high latitude regions (Asher et al., 2011; Pohlman et al., 2017; Kim et al., 2017). Zafiriou et al. (2008) and Conte et al. (2019) have also mentioned a potential influence of horizontal processes of different water masses on CO profiles in low latitude oligotrophic regions. Based on these studies, the horizontal transport could help explain the discrepancies in the observed CO budget in this study.

In the NP province, a typical exponential pattern of vertical gradients in dissolved $[\text{CO}]$ was observed at all stations (Fig. 6b). A pronounced decrease in $[\text{CO}]$ was evident within the surface mixed layer, indicating the photochemical degradation of CDOM following the penetration depth of short-wavelength radiation. However, due to the extensive spatial coverage of this province, there appear to be varying local-scale physical influences. In particular, stations 3 and 4 exhibited a relatively steep decline in CO concentration between the MLD and the layers below it compared with other stations. In these two stations, the lower layers showed slightly lower CO concentrations. In contrast, at other stations, the decline in CO concentration was less pronounced and the concentrations below the MLD were relatively higher. As shown in Fig. S7e, stations 3 and 4 had a larger difference in seawater temperature between the MLD and the lower layers, resulting in a greater density contrast. This suggests that these stations experienced less influence from diffusion below the mixed layer.

Additionally, the warm-core eddy signal was found at station 8 like at station 1 given that the CO concentrations at

depth are also high at the station. The slight increases in SST and SSS when passing through station 8 (Fig. 2f) imply the influence of warm-core eddy. Moreover, the two large eddies formed at both sides of station 8 in Fig. 1 also suggest the strong potential of the influences of those eddies. This is evidenced by the largest value of CB_{200} at station 8 among the stations in the NP due to high dissolved $[\text{CO}]$ in the water column, again pointing to the significant contribution of the lateral transport by subduction processes as well.

4 Summary and conclusions

Along the cruise track from the East Sea to the Bering Sea passing through the western limb of the North Pacific in summer 2012, we conducted the first-ever measurements of CO concentrations and relevant parameters in water columns. Dividing the cruise track into three provinces – the East Sea (ES), the North Pacific (NP), and the Bering Sea (BS) – we compared the CO cycles measured along the hydrographic stations. Photochemical production and microbial oxidation were the key drivers governing the CO budgets across the provinces while air–sea gas exchange and vertical transport played minor roles. The CO budgets were not balanced in the marginal seas, i.e., the ES and BS, while the open ocean (NP) exhibited a balanced budget. This highlights the significant contribution of physical transport, both in the marginal seas and potentially even in the open ocean on a local scale. To further investigate the imbalance of CO budgets, we calculated the CO column burden (CB_{200}). The CB_{200} was highest in the ES likely due to subduction of high-CO water into intermediate depths and a high production rate in the upper layers. The lowest CB_{200} in the BS stemmed from weak insolation and vigorous microbial oxidation. Despite greater removal than production, our observations suggest

that lateral transports of high-CO surface water supply CO in the surface layer in this area. Estimated external physical transports in the ES and BS, derived from imbalances in the CO budget, were 25 ± 17 and $40 \pm 19 \mu\text{mol m}^{-2} \text{d}^{-1}$, respectively. In contrast, the NP, where production and oxidation rates were approximately balanced, exhibited an intermediate CB_{200} value. In the NP, the influence of fluvial input or strong vertical mixing was observed at different geographical locations. Overall, our study highlights the significant role of physical transport in distributing CO in water columns, even in the open ocean, which should be considered in global ocean CO modeling efforts.

Data availability. All the datasets used in this paper are available at <https://doi.org/10.22663/KOPRI-KPDC-00002443.2> (Kwon et al., 2024).

Supplement. The supplement related to this article is available online at: <https://doi.org/10.5194/bg-21-1847-2024-supplement>.

Author contributions. YSK conducted measurements of CO concentration and the oxidation rate constant during the research cruise and wrote the initial draft of the manuscript. TSR developed the overall observational plan, designed the observation systems required for underway and discrete CO concentration measurements, and wrote the manuscript together with YSK. HCK provided CDOM data and HWK helped interpret physical oceanography, provided crucial insights, and conducted physical modeling experiments to support our hypotheses. All authors participated in the revision process and approved the final version of the paper.

Competing interests. The contact author has declared that none of the authors has any competing interests.

Disclaimer. Publisher's note: Copernicus Publications remains neutral with regard to jurisdictional claims made in the text, published maps, institutional affiliations, or any other geographical representation in this paper. While Copernicus Publications makes every effort to include appropriate place names, the final responsibility lies with the authors.

Acknowledgements. This study has been partially supported by the research programs “Survey of Geology and Seabed Environmental Changes in the Arctic Ocean (KIMST grant no. 20210632)” and a project on “the sustainable research and development of Dokdo (PG54141)”, which is funded by the Ministry of Oceans and Fisheries, Republic of Korea. This research project was carried out under the auspices of the SHIPPO program, which ran from 2012 to 2014. We thank the reviewers and editor for their helpful comments which improved the paper.

Financial support. This research has been supported by the projects “Sustainable Research and Development of Dokdo (PG54141)”, funded by the Ministry of Oceans and Fisheries, Republic of Korea, and “Survey of Geology and Seabed Environmental Changes in the Arctic Ocean”, funded by the Korea Institute of Marine Science and Technology Promotion (grant no. 20210632).

Review statement. This paper was edited by Hermann Bange and reviewed by two anonymous referees.

References

- Aagaard, K., Roach, A. T., and Schumacher, J. D.: On the wind-driven variability of the flow through Bering Strait, *J. Geophys. Res.-Oceans*, 90, 7213–7221, <https://doi.org/10.1029/JC090iC04p07213>, 2012.
- Asher, E. C., Merzouk, A., and Tortell, P. D.: Fine-scale spatial and temporal variability of surface water dimethylsulfide (DMS) concentrations and sea–air fluxes in the NE Subarctic Pacific, *Mar. Chem.*, 126, 63–75, <https://doi.org/10.1016/j.marchem.2011.03.009>, 2011.
- Bates, T. S., Kelly, K. C., Johnson, J. E., and Gammon, R. H.: Regional and seasonal variations in the flux of oceanic carbon monoxide to the atmosphere, *J. Geophys. Res.-Atmos.*, 100, 23093–23101, <https://doi.org/10.1029/95JD02737>, 1995.
- Bird, R. E. and Hulstrom, R. L.: Simplified clear sky model for direct and diffuse insolation on horizontal surfaces, Solar Energy Research Inst., Golden, CO (USA), <https://doi.org/10.2172/6510849>, 1981.
- Brenninkmeijer, C. A. M.: Measurement of the abundance of ^{14}C in the atmosphere and the $^{13}\text{C}/^{12}\text{C}$ and $^{18}\text{O}/^{16}\text{O}$ ratio of atmospheric CO with applications in New Zealand and Antarctica, *J. Geophys. Res.-Atmos.*, 98, 10595–10614, <https://doi.org/10.1029/93JD00587>, 1993.
- Bricaud, A., Morel, A., and Prieur, L.: Absorption by dissolved organic matter of the sea (yellow substance) in the UV and visible domains 1, *Limnol. Oceanogr.*, 26, 43–53, 1981.
- Capotondi, A., Jacox, M., Bowler, C., Kavanaugh, M., Lehodey, P., Barrie, D., Brodie, S., Chaffron, S., Cheng, W., Dias, D. F., Eveillard, D., Guidi, L., Iudicone, D., Lovenduski, N. S., Nye, J. A., Ortiz, I., Pirhalla, D., Pozo Buil, M., Saba, V., Sheridan, S., Siedlecki, S., Subramanian, A., de Vargas, C., Di Lorenzo, E., Doney, S. C., Hermann, A. J., Joyce, T., Merrifield, M., Miller, A. J., Not, F., and Pesant, S.: Observational Needs Supporting Marine Ecosystems Modeling and Forecasting: From the Global Ocean to Regional and Coastal Systems, *Front. Mar. Sci.*, 6, 623, <https://doi.org/10.3389/fmars.2019.00623>, 2019.
- Carder, K. L., Chen, F. R., Lee, Z. P., Hawes, S. K., and Kamykowski, D.: Semianalytic Moderate-Resolution Imaging Spectrometer algorithms for chlorophyll a and absorption with bio-optical domains based on nitrate-depletion temperatures, *J. Geophys. Res.-Oceans*, 104, 5403–5421, <https://doi.org/10.1029/1998jc900082>, 1999.
- Chen, J. L., Wilson, C. R., Blankenship, D., and Tapley, B. D.: Accelerated Antarctic ice loss from satellite gravity measurements, *Nat. Geosci.*, 2, 859–862, <https://doi.org/10.1038/ngeo694>, 2009.

- Conrad, R. and Seiler, W.: Photooxidative production and microbial consumption of carbon monoxide in seawater, *FEMS Microbiol. Lett.*, 9, 61–64, 1980.
- Conrad, R., Seiler, W., Bunse, G., and Giehl, H.: Carbon monoxide in seawater (Atlantic Ocean), *J. Geophys. Res.-Oceans*, 87, 8839–8852, 1982.
- Conte, L., Szopa, S., Séférian, R., and Bopp, L.: The oceanic cycle of carbon monoxide and its emissions to the atmosphere, *Biogeosciences*, 16, 881–902, <https://doi.org/10.5194/bg-16-881-2019>, 2019.
- Daniel, J. S. and Solomon, S.: On the climate forcing of carbon monoxide, *J. Geophys. Res.*, 103, 13249–13260, 1998.
- Day, D. A. and Faloon, I.: Carbon monoxide and chromophoric dissolved organic matter cycles in the shelf waters of the northern California upwelling system, *J. Geophys. Res.*, 114, C01006, <https://doi.org/10.1029/2007jc004590>, 2009.
- de Boyer Montégut, C.: Mixed layer depth over the global ocean: An examination of profile data and a profile-based climatology, *J. Geophys. Res.*, 109, C12003, <https://doi.org/10.1029/2004jc002378>, 2004.
- D'Sa, E. J., Goes, J. I., Gomes, H., and Mouw, C.: Absorption and fluorescence properties of chromophoric dissolved organic matter of the eastern Bering Sea in the summer with special reference to the influence of a cold pool, *Biogeosciences*, 11, 3225–3244, <https://doi.org/10.5194/bg-11-3225-2014>, 2014.
- Edson, J. B., Jampana, V., Weller, R. A., Bigorre, S. P., Plueddemann, A. J., Fairall, C. W., Miller, S. D., Mahrt, L., Vickers, D., and Hersbach, H.: On the Exchange of Momentum over the Open Ocean, *J. Phys. Oceanogr.*, 43, 1589–1610, <https://doi.org/10.1175/jpo-d-12-0173.1>, 2013.
- Erickson III, D. J.: Ocean to atmosphere carbon monoxide flux: Global inventory and climate implications, *Global Biogeochem. Cy.*, 3, 305–314, 1989.
- Fairall, C. W., Bradley, E. F., Hare, J. E., Grachev, A. A., and Edson, J. B.: Bulk Parameterization of Air–Sea Fluxes: Updates and Verification for the COARE Algorithm, *J. Climate*, 16, 571–591, [https://doi.org/10.1175/1520-0442\(2003\)016<0571:Bpoasf>2.0.Co;2](https://doi.org/10.1175/1520-0442(2003)016<0571:Bpoasf>2.0.Co;2), 2003.
- Ficht, C. G. and Miller, W. L.: An approach to quantify depth-resolved marine photochemical fluxes using remote sensing: Application to carbon monoxide (CO) photoproduction, *Remote Sens. Environ.*, 114, 1363–1377, <https://doi.org/10.1016/j.rse.2010.01.019>, 2010.
- Fujiki, T., Matsumoto, K., Mino, Y., Sasaoka, K., Wakita, M., Kawakami, H., Honda, M. C., Watanabe, S., and Saino, T.: Seasonal cycle of phytoplankton community structure and photophysiological state in the western subarctic gyre of the North Pacific, *Limnol. Oceanogr.*, 59, 887–900, <https://doi.org/10.4319/lo.2014.59.3.0887>, 2014.
- Gnanadesikan, A.: Modeling the diurnal cycle of carbon monoxide: Sensitivity to physics, chemistry, biology, and optics, *J. Geophys. Res.-Oceans*, 101, 12177–12191, <https://doi.org/10.1029/96jc00463>, 1996.
- Gros, V., Peeken, I., Bluhm, K., Zöllner, E., Sarda-Estève, R., and Bonsang, B.: Carbon monoxide emissions by phytoplankton: evidence from laboratory experiments, *Environ. Chem.*, 6, 369–379, <https://doi.org/10.1071/en09020>, 2009.
- Ho, D. T., Wanninkhof, R., Schlosser, P., Ullman, D. S., Hebert, D., and Sullivan, K. F.: Toward a universal relationship between wind speed and gas exchange: Gas transfer velocities measured with $^3\text{He}/\text{SF}_6$ during the Southern Ocean Gas Exchange Experiment, *J. Geophys. Res.*, 116, C00F04, <https://doi.org/10.1029/2010jc006854>, 2011.
- Ichiye, T. and Takano, K.: Mesoscale eddies in the Japan Sea, *Limnol. Oceanogr.*, 26, 69–75, 1988.
- Isobe, A.: Freshwater and temperature transports through the Tsushima-Korea Straits, *J. Geophys. Res.*, 107, 2-1–2-20, <https://doi.org/10.1029/2000jc000702>, 2002.
- Isoda, Y. and Saitoh, S.-i.: The northward intruding eddy along the East coast of Korea, *J. Oceanogr.*, 49, 443–458, <https://doi.org/10.1007/bf02234959>, 1993.
- Johnson, J. E.: Evaluation of a seawater equilibrator for shipboard analysis of dissolved oceanic trace gases, *Anal. Chim. Acta*, 395, 119–132, [https://doi.org/10.1016/S0003-2670\(99\)00361-X](https://doi.org/10.1016/S0003-2670(99)00361-X), 1999.
- Johnson, J. E. and Bates, T. S.: Sources and sinks of carbon monoxide in the mixed layer of the tropical South Pacific Ocean, *Global Biogeochem. Cy.*, 10, 347–359, <https://doi.org/10.1029/96gb00366>, 1996.
- Jones, R. D.: Carbon monoxide and methane distribution and consumption in the photic zone of the Sargasso Sea, *Deep-Sea Res. Pt.*, 38, 625–635, [https://doi.org/10.1016/0198-0149\(91\)90002-w](https://doi.org/10.1016/0198-0149(91)90002-w), 1991.
- Jones, R. D. and Amador, J. A.: Methane and carbon monoxide production, oxidation, and turnover times in the Caribbean Sea as influenced by the Orinoco River, *J. Geophys. Res.-Oceans*, 98, 2353–2359, <https://doi.org/10.1029/92JC02769>, 1993.
- Kettle, A. J.: A Model of the Temporal and Spatial Distribution of Carbon Monoxide in the Mixed layer, Massachusetts Institute of Technology, Massachusetts, USA, <https://dspace.mit.edu/bitstream/handle/1721.1/54397/3/1727109-MIT.pdf;sequence=2> (last access: 1 February 2015), 1994.
- Kettle, A. J.: Diurnal cycling of carbon monoxide (CO) in the upper ocean near Bermuda, *Ocean Model.*, 8, 337–367, <https://doi.org/10.1016/j.ocemod.2004.01.003>, 2005a.
- Kettle, A. J.: Comparison of the nonlocal transport characteristics of a series of one-dimensional oceanic boundary layer models, *Ocean Model.*, 8, 301–336, <https://doi.org/10.1016/j.ocemod.2004.01.002>, 2005b.
- Kim, C.-H. and Yoon, J.-H.: Modeling of the wind-driven circulation in the Japan Sea using a reduced gravity model, *J. Oceanogr.*, 52, 359–373, <https://doi.org/10.1007/bf02235930>, 1996.
- Kim, C.-H. and Yoon, J.-H.: A Numerical Modeling of the Upper and the Intermediate Layer Circulation in the East Sea, *J. Oceanogr.*, 55, 327–345, <https://doi.org/10.1023/a:1007837212219>, 1999.
- Kim, I., Hahm, D., Park, K., Lee, Y., Choi, J. O., Zhang, M., Chen, L., Kim, H. C., and Lee, S.: Characteristics of the horizontal and vertical distributions of dimethyl sulfide throughout the Amundsen Sea Polynya, *Sci. Total Environ.*, 584–585, 154–163, <https://doi.org/10.1016/j.scitotenv.2017.01.165>, 2017.
- Kinder, T. H., Coachman, L. K., and Galt, J. A.: The Bering Slope Current System, *J. Phys. Oceanogr.*, 5, 231–244, [https://doi.org/10.1175/1520-0485\(1975\)005<0231:Tbscs>2.0.Co;2](https://doi.org/10.1175/1520-0485(1975)005<0231:Tbscs>2.0.Co;2), 1975.
- Kitidis, V., Tilstone, G. H., Smyth, T. J., Torres, R., and Law, C. S.: Carbon monoxide emission from a Mau-

- ritanian upwelling filament, *Mar. Chem.*, 127, 123–133, <https://doi.org/10.1016/j.marchem.2011.08.004>, 2011.
- Kuroda, H., Suyama, S., Miyamoto, H., Setou, T., and Nakanowatari, T.: Interdecadal variability of the Western Subarctic Gyre in the North Pacific Ocean, *Deep-Sea Res. Pt. I*, 169, 103461, <https://doi.org/10.1016/j.dsr.2020.103461>, 2021.
- Kwak, J. H., Hwang, J., Choy, E. J., Park, H. J., Kang, D.-J., Lee, T., Chang, K.-I., Kim, K.-R., and Kang, C.-K.: High primary productivity and f-ratio in summer in the Ulleung basin of the East/Japan Sea, *Deep-Sea Res. Pt. I*, 79, 74–85, <https://doi.org/10.1016/j.dsr.2013.05.011>, 2013.
- Kwon, Y. S., Rhee, T. S., Kim, H. C., and Kang, H.-W.: Observations of Carbon Monoxide (CO) in the Western North Pacific and the Bering Sea in 2012, KOPRI [data set], <https://doi.org/10.22663/KOPRI-KPDC-00002443.2>, 2024.
- Ladd, C. and Stabeno, P. J.: Freshwater transport from the Pacific to the Bering Sea through Amukta Pass, *Geophys. Res. Lett.*, 36, L14608, <https://doi.org/10.1029/2009gl039095>, 2009.
- Lamontagne, R. A.: Distribution of Carbon Monoxide and C1-C4 Hydrocarbons in the Northeastern Portion of the Bering Sea During the Summer of 1977, Naval Research Laboratory, Washington, DC, 16, 1979.
- Levy II, H.: Normal atmosphere: large radical and formaldehyde concentrations predicted, *Science*, 173, 141–143, <https://doi.org/10.1126/science.173.3992.141>, 1971.
- Mahadevan, A., Lévy, M., and Mémerly, L.: Mesoscale variability of sea surface $p\text{CO}_2$: What does it respond to?, *Global Biogeochem. Cy.*, 18, GB1017, <https://doi.org/10.1029/2003GB002102>, 2004.
- Mannino, A., Novak, M. G., Hooker, S. B., Hyde, K., and Aurin, D.: Algorithm development and validation of CDOM properties for estuarine and continental shelf waters along the northeastern U.S. coast, *Remote Sens. Environ.*, 152, 576–602, <https://doi.org/10.1016/j.rse.2014.06.027>, 2014.
- Mathis, J. T., Hansell, D. A., and Bates, N. R.: Strong hydrographic controls on spatial and seasonal variability of dissolved organic carbon in the Chukchi Sea, *Deep-Sea Res. Pt. II*, 52, 3245–3258, <https://doi.org/10.1016/j.dsr.2.2005.10.002>, 2005.
- Miller, W. L., Moran, M., Sheldon, W. M., Zepp, R. G., and Opsahl, S.: Determination of apparent quantum yield spectra for the formation of biologically labile photoproducts, *Limnol. Oceanogr.*, 47, 343–352, <https://doi.org/10.4319/lo.2002.47.2.0343>, 2002.
- Mopper, K. and Kieber, D.: Marine photochemistry and its impact on carbon cycling, in: *The effects of UV radiation in the marine environment*, 101–129, ISBN 9781139429511, 2000.
- Morimoto, A., Takikawa, T., Onitsuka, G., Watanabe, A., Moku, M., and Yanagi, T.: Seasonal variation of horizontal material transport through the eastern channel of the Tsushima Straits, *J. Oceanogr.*, 65, 61–71, <https://doi.org/10.1007/s10872-009-0006-z>, 2009.
- Nakagawa, F., Tsunogai, U., Gamo, T., and Yoshida, N.: Stable isotopic compositions and fractionations of carbon monoxide at coastal and open ocean stations in the Pacific, *J. Geophys. Res.-Oceans*, 109, C06016, <https://doi.org/10.1029/2001JC001108>, 2004.
- Nightingale, P. D., Malin, G., Law, C. S., Watson, A. J., Liss, P. S., Liddicoat, M. I., Boutin, J., and Upstill-Goddard, R. C.: In situ evaluation of air-sea gas exchange parameterizations using novel conservative and volatile tracers, *Global Biogeochem. Cy.*, 14, 373–387, <https://doi.org/10.1029/1999gb900091>, 2000.
- Ohta, K.: Diurnal Variations of Carbon Monoxide Concentration in the Equatorial Pacific Upwelling Region, *J. Oceanogr.*, 53, 173–178, 1997.
- Omand, M. M., D’Asaro, E. A., Lee, C. M., Perry, M. J., Briggs, N., Cetinic, I., and Mahadevan, A.: Eddy-driven subduction exports particulate organic carbon from the spring bloom, *Science*, 348, 222–225, <https://doi.org/10.1126/science.1260062>, 2015.
- Park, K. and Rhee, T. S.: Source characterization of carbon monoxide and ozone over the Northwestern Pacific in summer 2012, *Atmos. Environ.*, 111, 151–160, 2015.
- Park, K. and Rhee, T. S.: Oceanic source strength of carbon monoxide on the basis of basin-wide observations in the Atlantic, *Environ. Sci. Process. Impacts*, 18, 104–114, <https://doi.org/10.1039/c5em00546a>, 2016.
- Parsons, T., Maita, Y., and Lalli, C.: *A manual of chemical and biological methods for seawater analysis*, Pergamon Press, Oxford, 173 pp., ISBN 9781483293394, https://books.google.co.kr/books?id=iAvBQAAQBAJ&dq=A+manual+of+chemical+and+biological+methods+for+seawater+analysis&lr=&hl=ko&source=gbs_navlinks_s (last access: 1 July 2013), 1984.
- Pathirana, S. L., van der Veen, C., Popa, M. E., and Röckmann, T.: An analytical system for stable isotope analysis on carbon monoxide using continuous-flow isotope-ratio mass spectrometry, *Atmos. Meas. Tech.*, 8, 5315–5324, <https://doi.org/10.5194/amt-8-5315-2015>, 2015.
- Pohlman, J. W., Greinert, J., Ruppel, C., Silyakova, A., Vielstade, L., Casso, M., Mienert, J., and Bunz, S.: Enhanced CO₂ uptake at a shallow Arctic Ocean seep field overwhelms the positive warming potential of emitted methane, *P. Natl. Acad. Sci. USA*, 114, 5355–5360, <https://doi.org/10.1073/pnas.1618926114>, 2017.
- Rhee, T. S.: The process of air-water gas exchange and its application, Texas A&M University College Station, Texas, USA, <https://www.proquest.com/openview/5773680793866702072976f78d7c5bb6/1?pq-origsite=gscholar&cbl=18750&diss=y> (last access: 1 July 2015), 2000.
- Rhee, T. S., Kettle, A. J., and Andreae, M. O.: Methane and nitrous oxide emissions from the ocean: A reassessment using basin-wide observations in the Atlantic, *J. Geophys. Res.-Atmos.*, 114, D12304, <https://doi.org/10.1029/2008JD011662>, 2009.
- Seiler, W. and Junge, C.: Carbon monoxide in the atmosphere, *J. Geophys. Res.*, 75, 2217–2226, <https://doi.org/10.1029/JC075i012p02217>, 1970.
- Shin, H.-R., Shin, C.-W., Kim, C., Byun, S.-K., and Hwang, S.-C.: Movement and structural variation of warm eddy WE92 for three years in the Western East/Japan Sea, *Deep-Sea Res. Pt. II*, 52, 1742–1762, <https://doi.org/10.1016/j.dsr.2.2004.10.004>, 2005.
- Sikorski, R. J. and Zika, R. G.: Modeling mixed-layer photochemistry of H₂O₂: Optical and chemical modeling of production, *J. Geophys. Res.-Oceans*, 98, 2315–2328, <https://doi.org/10.1029/92jc02933>, 2012.
- Smith, S. R., Bourassa, M. A., and Sharp, R. J.: Establishing More Truth in True Winds, *J. Atmos. Ocean. Tech.*, 16, 939–952, [https://doi.org/10.1175/1520-0426\(1999\)016<0939:Emitw>2.0.Co;2](https://doi.org/10.1175/1520-0426(1999)016<0939:Emitw>2.0.Co;2), 1999.

- Stabeno, P. J. and Reed, R.: Circulation in the Bering Sea basin observed by satellite-tracked drifters: 1986–1993, *J. Phys. Oceanogr.*, 24, 848–854, 1994.
- Stabeno, P. J., Schumacher, J. D., and Ohtani, K.: The physical oceanography of the Bering Sea, in: *Dynamics of the Bering Sea*, 1–28, https://people-new.ucsc.edu/~acr/migrated/BeringResources/Articlesofinterest/BeringSeageneral/dynamicsoftheberingsea_2_book.pdf (last access: 1 December 2021), 1999.
- Steinberg, D. K., Nelson, N., Carlson, C., and Prusak, A. C.: Production of chromophoric dissolved organic matter (CDOM) in the open ocean by zooplankton and the colonial cyanobacterium *Trichodesmium* spp, *Mar. Ecol.-Prog. Ser.*, 267, 45–56, <https://doi.org/10.3354/meps267045>, 2004.
- Stubbins, A., Uher, G., Kitidis, V., Law, C. S., Upstill-Goddard, R. C., and Woodward, E. M. S.: The open-ocean source of atmospheric carbon monoxide, *Deep-Sea Res. Pt. II*, 53, 1685–1694, <https://doi.org/10.1016/j.dsr2.2006.05.010>, 2006a.
- Stubbins, A., Uher, G., Law, C. S., Mopper, K., Robinson, C., and Upstill-Goddard, R. C.: Open-ocean carbon monoxide photoproduction, *Deep-Sea Res. Pt. II*, 53, 1695–1705, <https://doi.org/10.1016/j.dsr2.2006.05.011>, 2006b.
- Takao, S., Iida, T., Isada, T., Saitoh, S.-I., Hirata, T., and Suzuki, K.: Bio-optical properties during the summer season in the Sea of Okhotsk, *Prog. Oceanogr.*, 126, 233–241, <https://doi.org/10.1016/j.pocean.2014.04.010>, 2014.
- Twardowski, M. S., Boss, E., Sullivan, J. M., and Donaghay, P. L.: Modeling the spectral shape of absorption by chromophoric dissolved organic matter, *Mar. Chem.*, 89, 69–88, <https://doi.org/10.1016/j.marchem.2004.02.008>, 2004.
- Vodacek, A., Blough, N. V., DeGrandpre, M. D., DeGrandpre, M. D., and Nelson, R. K.: Seasonal variation of CDOM and DOC in the Middle Atlantic Bight: Terrestrial inputs and photooxidation, *Limnol. Oceanogr.*, 42, 674–686, <https://doi.org/10.4319/lo.1997.42.4.0674>, 1997.
- Vollmer, M. K., Walter, S., Mohn, J., Steinbacher, M., Bond, S. W., Röckmann, T., and Reimann, S.: Molecular hydrogen (H₂) combustion emissions and their isotope (D/H) signatures from domestic heaters, diesel vehicle engines, waste incinerator plants, and biomass burning, *Atmos. Chem. Phys.*, 12, 6275–6289, <https://doi.org/10.5194/acp-12-6275-2012>, 2012.
- Walvoord, M. A. and Striegl, R. G.: Increased groundwater to stream discharge from permafrost thawing in the Yukon River basin: Potential impacts on lateral export of carbon and nitrogen, *Geophys. Res. Lett.*, 34, L12402, <https://doi.org/10.1029/2007gl030216>, 2007.
- Wanninkhof, R.: Relationship between wind speed and gas exchange over the ocean, *J. Geophys. Res.-Oceans*, 97, 7373–7382, <https://doi.org/10.1029/92JC00188>, 1992.
- Wanninkhof, R.: Relationship between wind speed and gas exchange over the ocean revisited, *Limnol. Oceanogr.-Meth.*, 12, 351–362, <https://doi.org/10.4319/lom.2014.12.351>, 2014.
- Wanninkhof, R. and Thoning, K.: Measurement of fugacity of CO₂ in surface water using continuous and discrete sampling methods, *Mar. Chem.*, 44, 189–204, [https://doi.org/10.1016/0304-4203\(93\)90202-Y](https://doi.org/10.1016/0304-4203(93)90202-Y), 1993.
- Weinstock, B. and Niki, H.: Carbon monoxide balance in nature, *Science*, 176, 290–292, <https://doi.org/10.1126/science.176.4032.290>, 1972.
- Wiesenburg, D. A. and Guinasso, N. L.: Equilibrium solubilities of methane, carbon monoxide, and hydrogen in water and sea water, *J. Chem. Eng. Data*, 24, 356–360, <https://doi.org/10.1021/je60083a006>, 1979.
- Xie, H., Zafiriou, O. C., Umile, T. P., and Kieber, D. J.: Biological consumption of carbon monoxide in Delaware Bay, NW Atlantic and Beaufort Sea, *Mar. Ecol. Prog. Ser.*, 290, 1–14, <https://doi.org/10.3354/meps290001>, 2005.
- Xie, H. X. and Zafiriou, O. C.: Evidence for significant photochemical production of carbon monoxide by particles in coastal and oligotrophic marine waters, *Geophys. Res. Lett.*, 36, L23606, <https://doi.org/10.1029/2009gl041158>, 2009.
- Yamamoto-Kawai, M., Carmack, E., and McLaughlin, F.: Nitrogen balance and Arctic throughflow, *Nature*, 443, 43, <https://doi.org/10.1038/443043a>, 2006.
- Yamashita, Y., Cory, R. M., Nishioka, J., Kuma, K., Tanoue, E., and Jaffé, R.: Fluorescence characteristics of dissolved organic matter in the deep waters of the Okhotsk Sea and the northwestern North Pacific Ocean, *Deep-Sea Res. Pt. II*, 57, 1478–1485, <https://doi.org/10.1016/j.dsr2.2010.02.016>, 2010.
- Yasuda, I.: The origin of the North Pacific Intermediate Water, *J. Geophys. Res.-Oceans*, 102, 893–909, <https://doi.org/10.1029/96jc02938>, 1997.
- Yasuda, I.: Hydrographic Structure and Variability in the Kuroshio/Oyashio Transition Area, *J. Oceanogr.*, 59, 389–402, <https://doi.org/10.1023/A:1025580313836>, 2003.
- Zafiriou, O. C., Andrews, S. S., and Wang, W.: Concordant estimates of oceanic carbon monoxide source and sink processes in the Pacific yield a balanced global “blue-water” CO budget, *Global Biogeochem. Cy.*, 17, 1015, <https://doi.org/10.1029/2001gb001638>, 2003.
- Zafiriou, O. C., Xie, H., Nelson, N. B., Najjar, R. G., and Wang, W.: Diel carbon monoxide cycling in the upper Sargasso Sea near Bermuda at the onset of spring and in midsummer, *Limnol. Oceanogr.*, 53, 835–850, <https://doi.org/10.4319/lo.2008.53.2.0835>, 2008.
- Zhang, Y., Xie, H. X., Fichot, C. G., and Chen, G. H.: Dark production of carbon monoxide (CO) from dissolved organic matter in the St. Lawrence estuarine system: Implication for the global coastal and blue water CO budgets, *J. Geophys. Res.-Oceans*, 113, C12020, <https://doi.org/10.1029/2008jc004811>, 2008.